Plasma Transport Induced by the Stochastic Magnetic Field

Kubota, Tetsuyuki
Interdisciplinary Graduate School of Engineering Sciences, Kyushu University

Itoh, Sanae-I.
Research Institute for Applied Mechanics, Kyushu University

Yagi, Masatoshi
Research Institute for Applied Mechanics, Kyushu University

https://doi.org/10.5109/6786356

出版情報：Reports of Research Institute for Applied Mechanics. 44 (116), pp.19-53, 1998-10. 九州大学応用力学研究所
バージョン：

Plasma Transport Induced by the Stochastic Magnetic Field

By Tetsuyuki KUBOTA*1, Sanae-I. ITOH*2 and Masatoshi YAGI*2

The anomalous plasma transport induced by the stochastic magnetic field is studied to understand the disruption phenomena in the tokamak plasma. At first, the transport matrix which indicate the plasma transport in the stochastic magnetic field is formulated. For the formulation, the quasi-linear approximation for the diffusivity of the stochastic magnetic field line is used and the shifted Maxwellian is assumed to the particle distribution. Using this transport matrix the radial electric field formation, which is generated by the ambipolar condition,and the associated temperature profile is obtained. The temperature profile in the stochastic magnetic field becomes flat because of the rapid temperature diffusion. Next the temperature crash, i.e., the sawtooth oscillation and the giant ELM, is analyzed using the turbulence-turbulence transition model, which describes the transition between the state of the electrostatic turbulence and that of the electromagnetic turbulence. This transition has a hysteresis characteristics. When the state changes to the electromagnetic mode, the stochastic magnetic field appears and the temperature transport is enhanced. This transition model is included in the 1-D transport equation. To calculate this transport equation numerically the crash of the temperature profile and the propagation of the crash front (avalanche) are realized by this model. The collapse without a precursor oscillation is revealed.

Key Words: plasma, stochastic magnetic field, anomalous transport, sawtooth oscillation, giant ELM

1. Introduction

Research on controlled thermonuclear fusion has long been a world-wide project. Large tokamaks such as JET, JT-60U and TFTR are making remarkable progress toward a realization of fusion conditions in a confined plasma. Recently, JET has produced slightly in excess of 12 MW of fusion power using a deuterium -tritium plasma. However, there are still many problems to be solved for the realization of fusion reactor. For examples, understanding the physics of anomalous transport phenomena or disruptive phenomena in high temperature plasmas are important issues, since these phenomena are an obstacle to attain the Lawson's criterion [1].

In magnetically confined plasmas, various types of crash phenomena (disruptive phenomena) are observed such as the sawtooth [2]～[4], the edge localized mode (ELM) [5]～[7], the internal collapse [8] and so on. Such phenomena are essential and challenging problems in fusion research since they limit the attainable plasma performance. The study of the catastrophic phenomena observed in high temperature plasmas is also an academic problem of nonlinear and far-nonequilibrium systems.

The sawtooth crash is commonly observed in ohmically and/or additionally heated plasmas in the majority of tokamaks. The sawtooth oscillation is characterized by the initial slow growth of the central electron temperature followed by the temperature crash. The theoretical study has been done to understand the mechanism of the sawtooth crash. A focus is made on the dynamics of the $m=1$, $n=1$ helical mode (m and n are the poloidal and troidal mode numbers, respectively), i. e., Kadomatsev's magnetic reconnection model [9]. Resent experimental re-

*1 Interdisciplinary Graduate School of Engineering Sciences, Kyushu University

*2 Research Institute for Applied Mechanics, Kyushu University

sults, however, have posed some questions about Kadomtsev's magnetic reconnection model and about numerical simulations based on it. That is, one is the problem of the time scale of sawtooth crash and another is the partial reconnection not full reconnection of the magnetic flux. For examples, in large tokamaks such as JET, JT-60U, an observed crash time is much faster than that predicted by the reconnection model. Furthermore, on the TEXTOR tokamak, it has been observed that the safety factor q, which represents the pitch of the magnetic field, on the magnetic axis remains below unity during the sawtooth [10, 11]. It means that the temperature profile shows a fast flattening, while the magnetic structure only slightly changes during the crash. These finding have stimulated the search for a theory that could simultaneously treat the temperature crash and the slight change in the magnetic structure which occur in faster time scale than that of Kadomtsev's reconnection model.

A model based on the magnetic stochastization (magnetic braiding), which enhances the heat transport without causing the reconnection of $q=1$ magnetic field line [12]～[14], has been proposed. The stochastization occurs when the magnetic islands overlap with each other [15]～[17]. Such magnetic stochasticity can lead to a much enhanced particle and energy transport perpendicular to the mean magnetic field.

ELMs are considered as another example of crash phenomena in high temperature plasmas, where ELMs cause the pressure crash at the plasma edge. The ELM bursts are frequently observed during the high confinement mode (H-mode). In experiments, at least three types of ELMS are observed; type I (a giant ELM), type III and dithers [7]. A giant ELM is obtained near the threshold value of β-limit at the plasma surface. A simulation of giant ELMs has been performed assuming a short internal breakdown of the transport barrier [18]. Although the termination of transport barrier is usually discussed in relation with the linear magnethydorodynamics (MHD) stability [5, 6], there remains a difficulty to explain the sudden increase of magnetic fluctuation in the time scale of $O(10\mu s)$. Several theoretical attempts to analyze the giant ELM are still incomplete.

Recently, a model theory for the temperature collapse has been proposed based on a transition from the electrostatic turbulence, which is relevant to the low confinement mode (L-mode) and the H-mode, to the electromagnetic turbulence with braided magnetic field (we call this state as "M-mode") in the high-β plasmas [19]～[21]. In the M-mode state, the pressure gradient exceeds a critical value, and the associated smallscale magnetic islands satisfy the island overlap condition. This leads to the enhanced electron transport in comparison with the ion transport, causing the stronger turbulence. The hysteresis characteristics between the two state are taken into account in this model. Such a model has a potentiality to explain the fast growth and the discontinuity of the growth rate as the nonlinear modes. This model has been applied to the study of the sawtooth oscillation in 0-dimensional case and the sawtooth-like oscillation of the pressure gradient has been obtained [20]. It has been shown that the giant ELM could be explained by the theory based on the transition between the H-mode and the M-mode with the hysteresis characteristics [21].

In this thesis, the enhanced plasma transport induced by the stochastic magnetic field is considered and the disruptive phenomena is studied based on this model.

At first the plasma transport in the stocahstic magnetic field is analyzed by use of the Boltzmann equation which includes the effect of the magnetic stochasticity. Assuming the quasi-linear approximation for the diffusivity of the magnetic field line, the transport matrix is derived [22, 23]. By use of this transport matrix, the formation of the radial electric field is calculated and the associated temperature profile in the stochastic region is evaluated. The build up of radial electric field is shown to affect the transport coefficients as well asthe temperature gradients in that region.

Secondly the crash of the temperature profile is studied by applying the turbulence-turbulence transition model between the L-mode and the M-mode in a tokamak plasma [24, 25]. The turbulence-turbulence transition model is included to the1-dimensional energy transport code. The spatial and temporal evolutions of the heat transport are studied in the system where the hysteresis characteristics between the heat conductivity and the pressure gradient exist. The crash of the temperature profile, the propagation of the crash front and the sawtooth-like oscillation of the pressure gradient are realized by this model. Furthermore, the characteristics of the avalanche associated with the crash are clarified.

The turbulence-turbulence transition model between the H-mode and the M-mode is also applied to the analysis of the burst phenomena in the edge plasma. The hysteresis characteristics of the heat conductivity are incorporated into the 1-dimensional energy transport code and the dynamics of the edge temperature are studied. The pivot point, in which the temperature perturbation tends to be zero, is observed during the occurrence of the crash. The propagation of the crash front, the spreading of the M -mode region and the energy burst from the plasma edge are simulated.

This thesis is organized in following way. In Chapter 2, the collapse phenomena observed in experiments are reviewed and some theories of the anomalous plasma transport in the stochastic magnetic field are explained.

In Chapter 3, the transport coefficients in the stochastic magnetic field are studied. The 4×4 transport matrix is formulated, which describes the relation between the thermodynamic forces and the plasma fluxes. By using this transport matrix, the temperature profile and the radial electric field which is induced by the bipolar diffusion in the stocahstic magnetic field are obtained.

In Chapter 4, the 1-dimensional energy transport in the plasma core is studied. The turbulence-turbulence transition model between the L-mode and the M-mode are taken into account and the dynamics is solved. The avalanche associated with the crash of the temperature profile and the sawtooth-like oscillation of the pressure gradient are also shown.

In Chapter 5, the turbulence-turbulence transition model between the H-mode and the M-mode is applied to the transport study of the edge plasma. The 1-dimensional energy transport equations for electron and ion are solved. The avalanche processes and the appearance of a pivot point of the temperature profile during the crash are shown. The analysis of the energy burst is also done.

Finally, in Chapter 6, the results and future studies are summarized.

2. Review

The aime of this thesis is to analyze both the enhanced plasma transport and the collapse of the temperature profile induced by the magnetic stochasticity. In this chapter the examples of the experimental study on the temperature collapse are shown and the theoretical study of the magnetic stochasticity and of the anomalous transport are surveyed.

At first the experimental study of the temperature collapses, the sawtooth crash and the giant ELM are reviewed. Then the conventional model for the temperature crash is explained. Some difficulties of this model are discussed related with recent experimental observations. Next, a new theoretical model of the temperature collapse is described, on which this study is grounded. The property of magnetic stochasticity is briefly explained and the quasi-linear magnetic diffusion coefficient in a stochastic magnetic field is derived. Finally, a turbulence-turbulence transition model is introduced and two examples are shown. As a first example, the turbulence-turbulence transition model between the L-mode and the M-mode is incorporated into the transport equation and the results of the 0-dimensional analysis for the sawtooth crash are shown. As a second example, the turbulence-turbulence transition model between the H-mode and the M-mode is considered and the characteristics of the giant ELM predicted by the model are discussed.

2.1 Temperature collapse

2.1.1 Sawtooth crash

The sawtooth oscillation has been observed in many tokamaks since it had been found in the ST tokamak in the middle of 1970. In the ST tokamak, fluctuations inX-ray intensity which have shown a characteristic sawtooth behavior have been observed (Fig. 2.1) [2]. The soft X-ray intensity shows the information of the electron density and temperature. The X-ray fluctuations are caused by a fluctuation in either of these quantities, but predominantly temperature fluctuations.

In a theoretical model proposed by Kadomtsev for the sawtooth oscillation [9], the temperature at the plasma center increases slowly during the ramp-up phase of the current, because of the ohmic heating. As the results, the increase of the current density makes the safety factor, q, below unity in the central region. This instability is observed as a precursor of the rapid sawtooth disruption. It is hypothesized that the disruption occurs the result of a magnetic island growing at the $q=1$ surface which leads to a rapid reconnection of magnetic field lines. The reconnection leads to a stable configuration with $q>1$ all over the plasma column, simultaneously producing the observed flattening of the temperature and density profiles. This cycle is then repeated (Fig. 2.2).

Later on a detailed sawtooth activity has been observed in JET plasma by the measurements of soft X-ray and electron cyclotron emission (ECE), during the sawtooth collapse [4].

In the JET tokamak, the sawtooth collapse has been reported to occur without precursors and on a time scale faster than that expected from Kadomtsev's model.

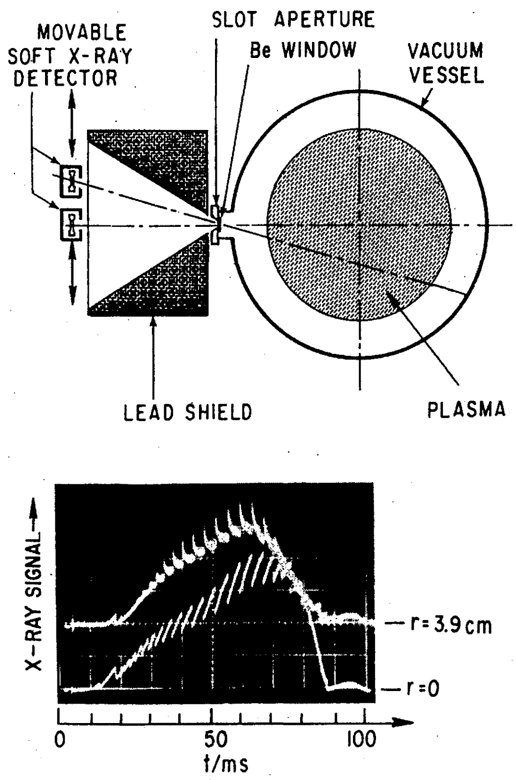

Fig. 2.1 The X-ray traces exhibit internal disruption. (Cited from Fig.1 in Ref.2)

The signal from a central X-ray detector has shown the large-amplitude sawtooth oscillations without precursors (Fig. 2.3). The expanded trace from the central detector shows a very rapid collapse occurring in $\sim 100\mu s$, which is significantly shorter than the time predicted theoretically, that is, $\sim 10ms$.

Recently, the Faraday rotation diagnostic technique, which is a direct method of detecting the change of the magnetic field structure, has become available and added a new picture in addition to the fact that the safety factor q remains below unity during the sawtooth oscillation [10, 11].

A typical result for an ohmic discharge in TEXTOR is shown in Fig. 2.4, where the upper three traces represent an interferometric phase shift which indicates the growth of the magnetic island and the lower trace is the Faraday rotation signal of the horizontal polarimetric probing beam which shows the sift of the magnetic axis. From the experimental result, the shift of the magnetic axis is estimated as 5.4cm corresponding to about one third of the radius $q=1$ surface. Thus, it is clear that the growth of the $m=n=1$ perturbation prior to a sawtooth collapse is insufficient to push the magnetic axis to the $q=1$ surface.

These experimental results at JET and TEXTOR pose a question about the magnetic

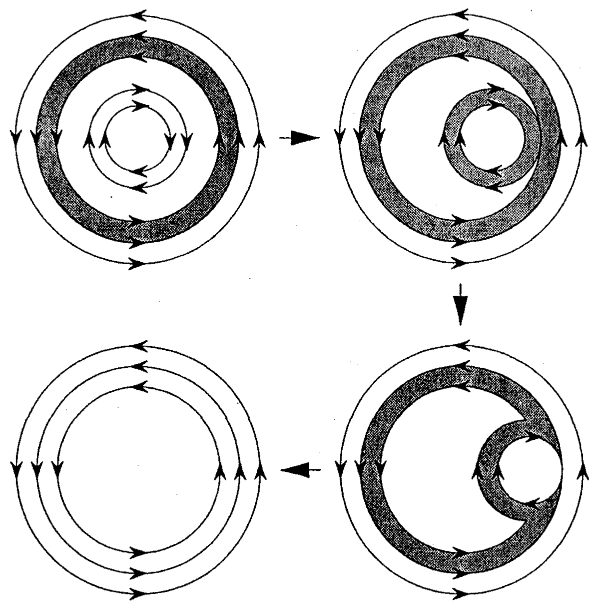

Fig. 2.2 Time evolution of helical flux surfaces during the full reconnectin process.

reconnection model for the sawtooth oscillation. Namely the crash time predicted by the Kadomtsev's magnetic reconnection model is about 100 times longer than the experimental results, and the shift of the magnetic axis obtained by the Faraday rotation is smaller than that for the full collapse. The Kadomtsev's model and the studies based on it seem to be insufficient to explain the sawtooth crash.

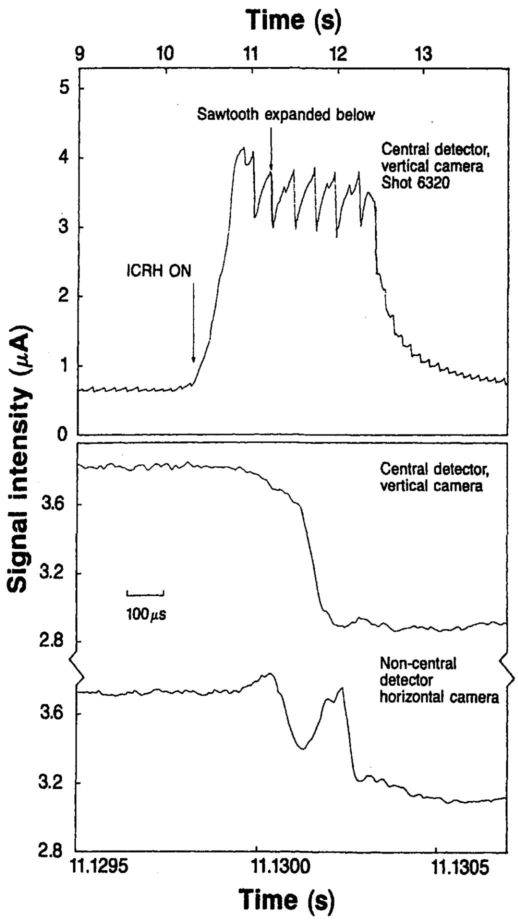

Fig. 2.3 X-ray signal intensity as a function of time. The lower two traces have the very expanded time scale.
(Cited from Fig.1 in Ref.4)

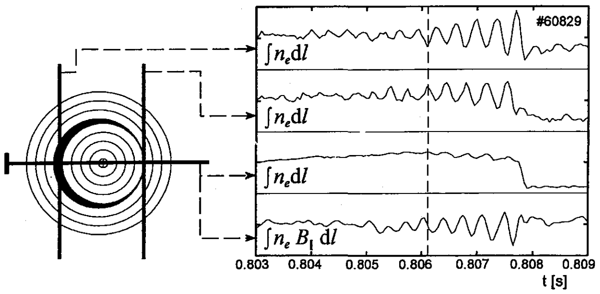

Fig. 2.4 Schematic illustration of a growing m =1 magnetic island and of the corresponding Faraday rotation to be detected by a horizontal polarimetric probing beam.
(Cited from Fig.4 in Ref.11)

2.1.2 ELMs

Bursts of edge localized modes (ELMs) [5,7] are frequently observed during the H-mode phase. ELMs are classified into the three types according to the occurrence of the magnetic precursor and the dependence of the ELM frequency on the energy flux through the separatrix, P_{sep}. The classes of the ELM are as follows.

● Type I ELMs (giant ELMs). The ELM repetition frequency ν_{ELM} increases with the energy flux through the separatrix:

$$\frac{d\nu_{ELM}}{dP_{sep}}>0. \tag{2.1}$$

The burst occurs near the ideal ballooning limit. No clear coherent magnetic precursor oscillation has been identified.

●Type III ELMs. The ELM repetition frequency decreases with the energy flux through the separatrix:

$$\frac{d\nu_{ELM}}{dP_{sep}}<0. \tag{2.2}$$

A coherent magnetic precursor oscillation of toroidal mode number $n=5\sim10$ and poloidal mode number $m=10\sim15$ is observed on magnetic probes located close to the plasma, especially in the outboard midplane.

● Dithering cycles. For $P_{sep}\approx P_{thr}^{LH}$, repetitive L-H-L transitions may occur, where P_{thr}^{LH} is the power threshold of the L-H transition. The repetition frequency shows a slight decrease with increasing P_{sep}. Dithering cycles show no magnetic precursor oscillation; the level of turbulence during the temporary L-mode does not significantly exceed that of the L-phase at $P_{sep}\leq P_{thr}^{LH}$.

Figure 2.5 shows the input power and the D_α-signal at the divertor for the typical sequence of ELMs during a power rise in DIII-D. Here D_α-signal resents the energy flux from the plasma surface. In a discharge where the heating power is increased in step, type III ELMs occur at heating power close to PLHthr, their frequency decreasing as P increases until an ELM-free Phase appears. At even higher P, type I ELMs (giant ELMs) occur, their frequency now increases with P and the time scale of the crash becomes the order of $10\mu s$.

The ideal MHD instability analysis has been performed to explain the giant ELMs. The ideal ballooning mode is supposed to be a candidate to dictate the stability boundary [26]. In this analysis, the edge pressure gradient builds up until the pressure gradient reaches a threshold value, then, a giant ELM occurs. However, the linear MHD analysis cannot explain either the abrupt change of the growth rate of magnetic perturbations or the dynamics of the crash phase.

2.2 Theoretical models of temperature collapse

As mentioned in the previous section, it is known that the conventional theoretical models are insufficient to explain the sudden temperature collapse, i.e., the sawtooth crash and the giant ELMs.

Recently, a model for the collapse phenomena has been proposed [20, 21]. This model asserts that the temperature collapse and its repetition are caused by the onset of the magnetic stochasticity and the hysteresis characteristics of the transport coefficients.

In this section, we review characteristics of the magnetic stochasticity, and introduce a related anomalous transport model, in which the hysteresis characteristics of the transport coefficient are taken into account.

2.2.1 Stochastic magnetic field

A Hamiltonian formalism is used to describe the behavior of magnetic field line because the magnetic field line can be regarded as the preservation system [17]. When there are nested toroidal flux surfaces, the field line trajectories are integrable, and the Hamiltonian which corresponds to the toroidal flux is formulated. Only very special configurations are integrable, and any perturbations to an integrable system will destroy the integrability. The problem is solved by use of the perturbation method. The primary effect is the occurrence of magnetic islands at every rational surface, on which the magnetic field line closes and the safety factor, q, equals to m/n, where each line on the surface closes on itself after m toroidal and n poloidal circuits. When the perturbation increases, the high order islands appear around the primary island. When the island sizes become comparable to their separation, they overlap with each other, that is called Chirikov criterion [27], and the nonlinear interaction causes the field lines to become stochastic. Figure 2.6 shows the evolution of the trajectory of the magnetic field lines in a

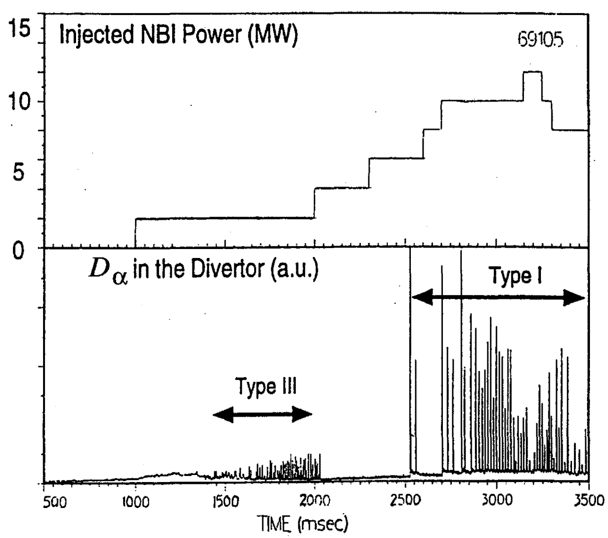

Fig. 2.5 Typical sequence of ELMs during a power rise in DIII-D: at $P_{sep} \approx P_{thr}^{LH}$, type III ELMs are found, at higher P, type I ELMs (giant ELMs) occur (Cited from Fig.2 in Ref.7).

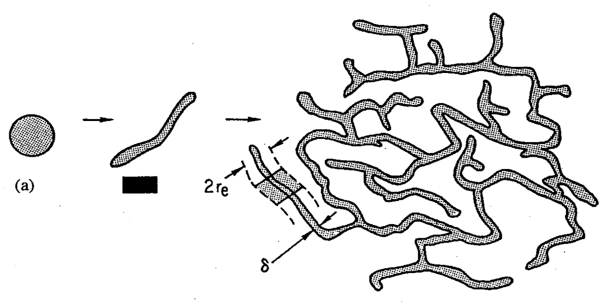

Fig. 2.6 The evolution of area mapping. Moving the small circle along the trajectory, this small circle is mapped into a complicated thin region and the width δ of the area exponentially decreases in order to conserve the total area. (Cite from Fig.1 in Ref.14)

stochastic magnetic field. The circle area is taken in the magnetic field (Fig. 2.6(a)). This area is deformed followed with the change of the magnetic field lines when the area moves along the direction of the mean magnetic field. If the magnetic field is not stochastic, then the area is only stretched to the poloidal direction. However, once the magnetic field becomes stochastic, the area becomes much complicated (Fig. 2.6(c)). In the stochastic magnetic field, the total area evolves as $l(z)=l_0\exp(z/Lc)$, where z is taken along the direction of the mean toroidal field and Lc is the correlation length. The wide δ of the area, $\delta(z)=10\exp(-z/Lc)$, exponentially decreases in order to conserve the total area. All processes of mapping are strictly reversible, but because the area becomes extraordinarily extensive, any small spreading perpendicular to the field line can be of great importance of the particle diffusion.

When a Hamiltonian system is far from the integrable limit (i. e., the magnetic stochasticity appears), the statistical approaches can be used to treat the effect of stochastic trajectories. The simplest approach is to use a quasi-linear theory leading to a diffusion coefficient depending only on the mean square level of the perturbing forces. The radial diffusion of magnetic field lines indicates the corresponding particle diffusion since the plasma particle is frozen in the magnetic field lines in the collisionless limit. Next we review the effect of magnetic turbulence on the transport.

2.2.2 Quasi-linear diffusion coefficient of the magnetic field line

When the magnetic field lines are stochastic, the particle is no longer confined within the flux surface. This is because the flux surface is distruced by the stochastic field. In a collisionless limit, particles are frozen in the magnetic field line, so that we can use the magnetic diffusion coefficient to estimate atest-particle diffusion coefficient.

The trapped particles are much perturbed by the turbulence of the magnetic field lines [28]. The particle diffusion in the stochastic magnetic field is represented by the quasi-linear formalism. The mean magnetic field B and the perturbed magnetic field B_x, which is perpendicular to the mean magnetic field, are assumed to be given, where x and z axes are taken along the direction of the perturbation and the mean magnetic field line, respectively (Fig. 2.7). It is assumed that plasma particles move with constant velocity v_z along the magnetic field lines. The particle diffusivity D_p along x axis is described as

$$D_p=v_zD_M, \tag{2.3}$$

where D_M is the diffusivity of the magnetic field lines which is defined as

$$D_M=\int_{-\infty}^{\infty}ds\langle b(\mathbf{r}(s),s)b(\mathbf{r}(0),0)\rangle, \tag{2.4}$$

$$b(\mathbf{r},s)=B_x(\mathbf{r},s)/B. \tag{2.5}$$

The correlation between the $b(\mathbf{r}(s), s)$ and $b(\mathbf{r}(0), 0)$ decays while the particle moves a distance of s away along the braided magnetic field lines (Fig. 2.7). Therefore the integration length is limited from 0 to L_s in the Eq. (2.4). If the amplitude of magnetic perturbation is small enough, the correlation of the magnetic field is estimated as $\langle b(\mathbf{r}(s), s)\, b(\mathbf{r}(0), 0)\rangle =b^2$. The magnetic field line diffusivity is obtained as

$$D_M=b^2L_s. \tag{2.6}$$

The particle diffusion in the perpendicular direction in the stochastic magnetic field is proportional to D_M, being represented by the quasilinear formalism. If the amplitude of the magnetic perturbation is large (strong turbulence limit),the magnetic field line diffusivity is estimated as $D_M \propto b$[19].

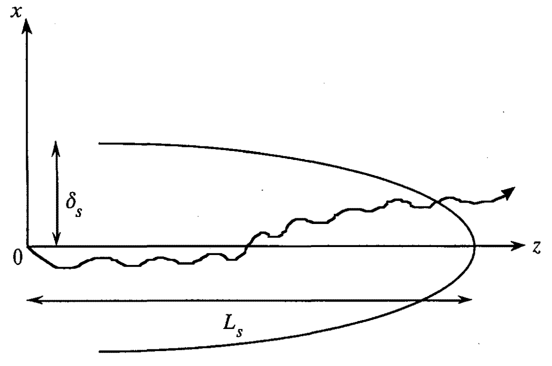

Fig. 2.7 The relation between the correlation length and the particale diffusion. Inside the elliptic line, the particle correlates with the turbulence. The correlation decays when the particle moves Ls away from the orgin. (Cited from Fig.5 in Ref.28)

The radia transort is caused by the parallel particle motion in destroyed magnetic surfaces. The electrn heat conductivity in the stochastic magnetic field is described as $\chi_e \sim D_M v_{Te}$, where v_{Te} is the electron thermal velocity [14].

2.2.3 Turbulence-turbulence transition model

• L-M transition model for the sawtooth oscillation

Recently, a new approach to magnetic turbulence and transport in toroidal plasma has been proposed [20]. The nonlinear interaction in electron dynamics leads to a nonlinear instability, which gives rise to the anomalous electron viscosity μ_e. The balance between the stabilization effects of the heat conductivity χ, the anomalous ion viscosity μ_i and the destabilization effect of μ_e determines the stationary turbulence and anomalous transport. This turbulence belongs to the strong turbulence. The theory of self-sustained turbulence has been also applied to a turbulence with the magnetic braiding in toroidal plasmas [19]. It has been found that, if the pressure gradient exceeds a certain threshold value, the self-sustainment of magnetic stochasticity occurs, causing the higher heat conductivity. The state is called the M-mode (magnetic braiding mode). Taking the interchange mode turbulence, the analytical formulae for χ, the magnetic perturbation amplitude and the threshold pressure gradient have been obtained. The dependence of χ on the pressure gradient and on the magnetic structure has been clarified. The electron heat conductivity, χ_e increases at most by a factor of m_i/m_e, where m_i and m_e are the ion and electron masses, respectively. The ion heat conductivity χ_i enhances at most by a factor of $\sqrt{m_i/m_e}$. The heat conductivity in the L-mode plasma is given as [19]

$$\chi^{L}_{e,i}=A\frac{(G_{0i}+G_{0e})^{3/2}}{s^2}\frac{c^2}{\omega_P^2}\frac{v_A}{R} , \tag{2.7}$$

and the heat conductivities in the M-mode are given as

$$\chi^{M}_{e}=A\frac{\left\{G_{0i}+G_{0e}\sqrt{\frac{m_eT_i}{m_iT_e}}\right\}^{3/2}}{s^2}\frac{c^2}{\omega_P^2}\frac{v_A}{R}\frac{m_iT_e}{m_eT_i} , \tag{2.8}$$

and

$$\chi^{M}_{i}=A\frac{\left\{G_{0i}+G_{0e}\sqrt{\frac{m_eT_i}{m_iT_e}}\right\}^{3/2}}{s^2}\frac{c^2}{\omega_P^2}\frac{v_A}{R}\sqrt{\frac{m_iT_e}{m_eT_i}} , \tag{2.9}$$

where the superscripts L and M indicate the L-mode and the M-mode and $G_{0i,e}$ denotes the normalized equilibrium pressure gradient coupled to the magnetic curvature,

$$G_{0i,e}=\frac{R}{a}\frac{d\ \ln\ B}{d\ \ln\ r}R\frac{d\beta_{0i,e}}{dr} , \tag{2.10}$$

a and R are the minor and major radii, v_A is the Alfvén velocity $v_A=B/\sqrt{\mu_0 m_i n_i}$, s is the shear parameter $s=r(dq/dr)q^{-2}$, ω_p is the plasma frequency $\omega_p=\sqrt{\frac{n_e e^2}{\varepsilon_0 m_e}}$ (e and ε_0 are the electron charge and the permittivity of free space), c is the light speed and β_0 is the total plasma beta $\beta_0=2\mu_0 p_0/B^2$ (p_0 is the total plasma pressure). The coefficient A is chosen by comparing χ to the experimental observations and in this case $A=12$ is chosen.

In this model, the magnetic fluctuations have the nature of a cusptype catastrophe. And the heat conductivities have hysteresis characteristics. The threshold value at which the transition from the L-mode to the M-mode occurs is calculated from the Chirikov condition for magnetic braiding and is given as

$$G_0>G_c\approx 0.5s , \tag{2.11}$$

and one of the transition from the M-mode to the L-mode is given as

$$G_0<G_1\approx 1.7\beta_i , \tag{2.12}$$

where $G_0=G_{0i}+G_{0e}$. Figure 2.8 shows the hysteresis curve of the transport coefficient.

For the explanation of the sawtooth oscillation, the 0-dimensional analysis of the heat transport has been done by use of this model. The dynamical change of the pressure gradient and the heat conductivity have been examined [20].

Figure 2.9 illustrates the dynamic behavior at the sawtooth crash. At the time $t=0$, the pressure gradient reaches the critical condition of the transition from the L-mode to the M-mode which is indicated by Eq. (2.11). The stochasticity, due to the magnetic braiding, is switched on, and the heat conductivity starts to increase in the time scale of $10\tau_{Ap}$, Where τ_{Ap} is the poloidal Alfven time $\tau_{Ap}=\sqrt{\mu_0 m_i n_i}/B_p$ (B_p is the poloidal magnetic field). The electron heat conductivity is enhanced and the electron pressure crashes in the time scale of $O(\tau_{Ec} m_i/m_e)$, where τ_{Ec} is the energy confinement time in the core region of the L-mode ($\tau_{Ec} \approx r_c^2/\chi^L$) and r_c is the minor radius at which the crash happens. The ion heat conductivity is also enhanced, and the ion pressure gradient is subject to the crash as well. The burst in the turbulence and the anomalous transport continue until the total pressure is reduced to the level of Eq.(2.12). Therefore the crash time of ion pressure gradient, $O(\tau_{Ec} m_i/m_e)$, determines the duration of the burst. The duration time is a few hundred times of τ_{Ap}. After the enhanced turbulent state terminates, the plasma pressure starts to increase, according to the L-mode conductivity. This sequence is repeated periodically, and is seen as the sawteeth. Figure 2.10 demonstrates the long-time evolution for the calculation of Fig. 2.9.

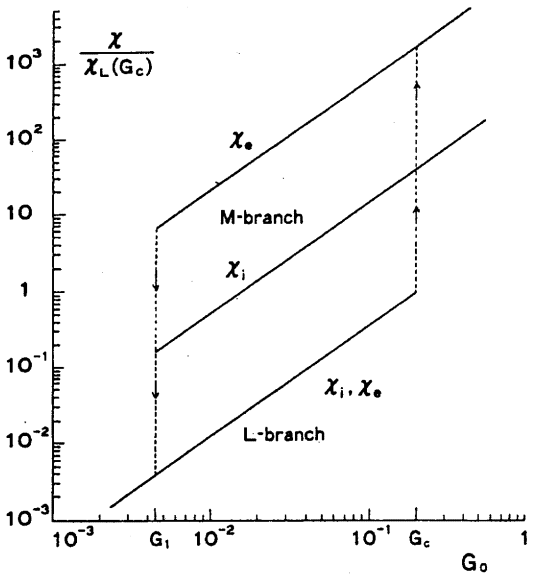

Fig. 2.8 Heat conductivity as a function of the pressure gradient. χ against G_0 is shown. The electron pressure gradient and ion pressure gradient are taken to be equal. At critical values of the gradient, G_c and G_1, a bifurcation takes place. The jump from the L- to M-branch and that from the M- to L-branch occur at $G_0=G_c$ and $G_0=G_1$, respectively.
(Cited from Fig.1 in Ref.20)

• H-M transition model for the giant ELM

This turbulence-turbulence transition model has also been applied to the giant ELM [21]. In [21], the theory of the self-sustained turbulence of the current-diffusive ballooning mode has been developed in the presence of a steep pressure gradient and a radial

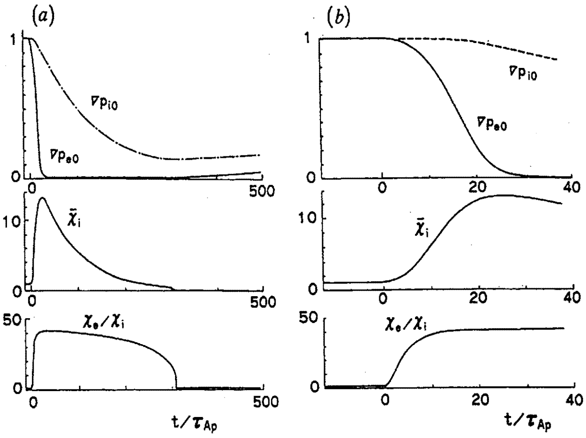

Fig. 2.9 Temporal evolution at the crash. The normalized pressure gradient (top), the ion thermal conductivity (middle) and the ratio of χ_e/χ_i (bottom) are shown. In (a), the change during the whole burst is shown. At time $t=0$, stochasticity occurs, and the crash starts. The magnetic braiding terminates at $t/\tau_{Ap} \simeq 300$, and the pressure gradient starts to increase again. The expanded view near the onset of the crash is shown in (b).
(Cited from Fig.2 in Ref.20)

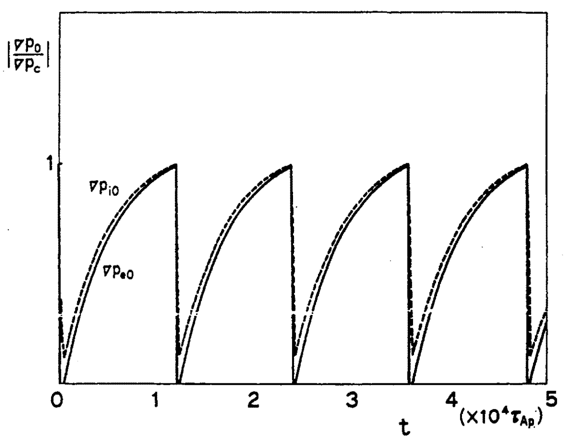

Fig. 2.10 Long time evolution for the calculation of Fig.2.9. The periodic crash and build-up of the pressure gradient are demonstrated. (Cited from Fig.3 in Ref.20)

electric field shear. Multifold states for the L-mode, H-mode and M-mode have been obtained. The heat conductivities for the H- and L-modes are derived as follows,

$$\chi_H=\frac{\chi_L}{1+G(s,\alpha)\omega_{E1}^2}\ , \tag{2.13}$$

$$\chi_L=\frac{\alpha^{3/2}}{g(s,\alpha)}\frac{\delta^2}{\tau_{Ap}}\ , \tag{2.14}$$

where $\omega_{E1}=(dE_r/dr)\ \tau_{Ap}/B$, $\alpha=-q^2Rd\beta/dr$ is the normalized pressure gradient, E_r is the radial electric field, the coefficients g and G are given as

$$g(s,\alpha)=(1+2\alpha-2s)\sqrt{2+3(s-\alpha)^2/\left(\frac{1}{2}+\alpha-s\right)}\ , \tag{2.15}$$

$$G(s,\alpha)=\frac{9}{8}\left(1+\frac{4}{3\alpha f}\right)^2\frac{\alpha}{f^2}+\frac{25(s-\alpha)^2}{4(1+2\alpha-2s)}\left(\frac{2+C}{1-C}\right)^{1/2}\times\left(1+\frac{4}{3\alpha f}\right)\left(1+\frac{4}{5\alpha f}\right)\frac{\alpha}{f^2}\ , \tag{2.16}$$

where $C=3(s-\alpha)^2(1/2+\alpha-s)^{-1}$ and $f=(1+2\alpha-2s)\sqrt{2+C}$. In the M-mode, the electron and ion heat conductivities are enhanced as

$$\chi_e^M=\sqrt{\frac{m^i}{m_e}}M\chi_i^M\ , \tag{2.17}$$

$$\chi_i^M=\sqrt{\frac{m^i}{m_e}}M\chi_{H,L}\ , \tag{2.18}$$

The coefficient M denotes the numerical factor $(0<M<1)$ indicating the effective rate of stochastization. In Eqs. (2.8) and (2.9), $M=1$ is assumed [19]. The threshold condition between the H-mode and the M-mode has been obtained. When α reaches α_c^H, the fluctuating islands overlap, where α_c^H is given as

$$\alpha_c^H\equiv\frac{\sqrt{g}}{2}(1+G\omega_{E1}^2)^{5/4}\left(1+s^2g^{-1}\sqrt{1+G\omega_{E1}^2}\ \right)^2\ , \tag{2.19}$$

The condition of the back-transition from the M-mode to the H-mode is given as

$$\alpha<\frac{g}{s^2}\frac{1}{\sqrt{1+G\omega_{E1}^2}}\beta_i\ . \tag{2.20}$$

A schematic diagram of the various branches is shown in Fig. 2.11. The Chirikov criterion for an H-M transition is plotted on the $s-\alpha$ plane (called a $s-\alpha$ diagram) for $\omega_{E1}=0.1$ and $\omega_{E1}=0.5$ (Fig 2.12). The stability boundary of the linear ideal MHD ballooning mode is also plotted for the reference. It is shown that the critical boundary is close to the condition for linear instability.

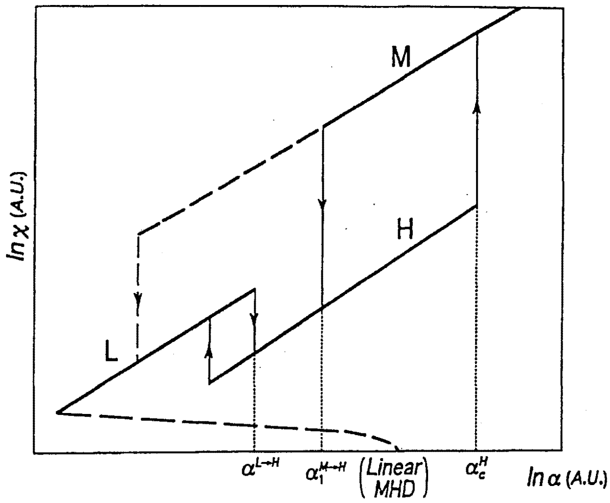

Fig. 2.11 Multifold solution of the self-sustained turbulence. The heat conductivity is shown as a function of the pressure gradient parameter α. (Cited from fig.1 in Ref.21)

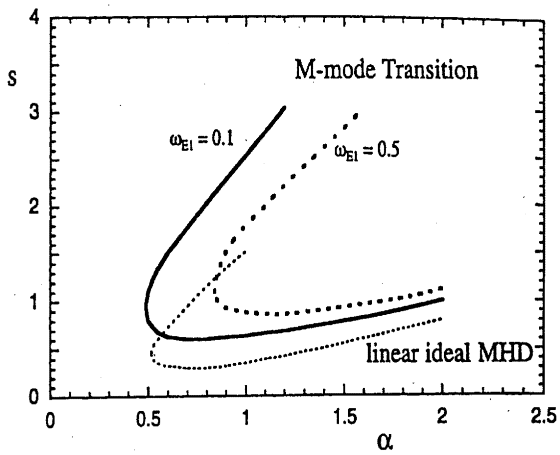

Fig. 2.12 The critical pressure gradient for the M-mode transition in $s-\alpha$ diagram. (Cited from Fig.4 in Ref.21)

3. Transport matrix and electric field formation in stochastic magnetic field

In this chapter we study the anomalous transport of a high temperature plasma ina stochastic magnetic field. The plasma transport matrix in the stochastic region is formulated under the assumption of quasi-linear approximation for the diffusivity of the magnetic field line. By use of this transport matrix the radial electric field formation and the associated density and temperature profiles in the stochastic region are obtained.

3.1 Introduction

The anomalous transport in the presence of a stochastic magnetic field has received considerable attention [12]. The research work has been done for the explanation of the electron thermal conductivity in toroidal devices [13, 14]. This mechanism is important since the heat flows rapidly perpendicular to the mean magnetic field line. The heat is carried by particles at their thermal speed without collisions, and thus principally by electrons. From the view point of the plasma confinement, the stochastic magnetic field has received considerable attention. However, we do not have sufficient understanding of the plasma transport in the stochastic magnetic field region. Other than the thermal conductivity [9], [29] [31] not enough attention has been paid on the electron viscosity [32], i.e., hyper resistivity [33]. The derivation of the elements in the form of transport matrix has rarely been done.

Furthermore, the radial electric field has also received strong attention in connection with the enhanced confinement [34]. What has been found in experiments is the existence of not only the edge electric field in the H-mode (High confinement mode) discharges, but also the internal electric field structure in another enhanced mode [35]. The reason why such radial electric field exists is not yet clear. The contribution from the diffusion in the stochastic magnetic field is a candidate, since the particle diffusion is intrinsically bipolar which many cause the radial electric field. The formulation of the transport matrix in the presence of the stochastic magnetic field will give a basis to understand the transport process as well as the global mode stability of toroidal plasmas.

In this chapter, we calculate the transport matrix elements for cylindrical plasma in a stochastic magnetic field. In a collinsionless limit, quasilinear approximation is used for the amplitude of the magnetostatic perturbation. We consider the relation of the plasma fluxes and the thermodynamic forces. The elements including the off-diagonal terms are derived. As an application, a formation of static electric field and the associated temperature distribution are analyzed. Here we will focus on the ambipolar electric field due to the particle diffusion, on the thermal conduction, and on the parallel thermoelectrc field caused by the thermal conduction. We also consider the effect of the ambipolar electric field on the plasma transport, where this electric field causes the $E\times B$ drift and drives the momentum flux.

The organization of this chapter is as follows. In section 3.2, the 4×4 transport matrix for each species will be derived. Using the derived coefficients, the formation of electric field, temperature distribution and the effect of the $E\times B$ drift are examined in section 3.3. Summary and discussion will be given in section 3.4.

3.2 Formulation of transport matrix

In this section, we present our theoretical model and formulae of the anomalous particle, momentum and energy fluxes due to magnetostatic turbulence, i. e., magnetic stochasticity. We consider a cylindrical plasma immersed in a strong magnetic field in the z-direction. The poloidal magnetic field is assumed to be small. Even in the presence of the magnetic braiding, the strength of the field is represented by the ensemble averaged value. The plasma is inhomogeneous in the radial direction.

We start our analysis with the kinetic equation which has been used to derive the thermal diffusivity and the current diffusivity [17] and extend the argument in the following. When the gyro-radius, ρ, is small compared with the inhomogeneity scale lengths, the kinetic equation for electrons and ions in the presence of magnetic stochasticity can be written as,

$$\frac{\partial f}{\partial t}+\mathbf{v}\cdot\nabla f+\frac{q}{m}(\mathbf{E}+\mathbf{v}\times\mathbf{B})\cdot\nabla_{v}f$$
$$=\frac{\partial}{\partial x}(|v_{||}|D_M)\frac{\partial f}{\partial x}+C(f)\ , \tag{3.1}$$

where $C(f)$ is a collision operator, and $D_M=(\delta r)^2/(2\pi R_0)$ indicates the diffusivity of the magnetic field line in the presence of stochasticity, where the field line takes random walks at the distance $\delta r=(\tilde{B}/B)2\pi R_0$ in going once around the torus. Quantities $\tilde{B}$, B and R_0 are the fluctuation amplitude of the magnetic field line, equilibrium magnetic field and major radius, respectively. Here we restrict to the collisionless limit, and use the quasi-linear value for D_M. We assume the D_M is uniform within the region of interest. The effect of the magnetic fluctuation is contained in the first term of the right hand of Eq. (3.1). Therefore we analyze the term for magnetic stochasticity.

To obtain matrix elements we shall take the moments of Eq. (3.1), specifying the unperturbed velocity distribution function. The plasma is assumed to be in a steady state. Thus the velocity distribution f_{0j} is a function of the energy, $m_jv^2/2+q_j\phi$, where ϕ is the static potential, and canonical momenta in the θ and parallel directions, $P_{\theta j}=m_jr(v_{\theta j}+r\Omega_j/2)$, where Ω_j is the cyclotron frequency, and $P_{||j}=m_jv_{||j}$, respectively. More specifically, we adopt a local Maxwellian distribution as

$$f_{0j}=f_{0\perp j}\cdot f^{0||j}\ ,$$
$$f_{0||j}=\frac{1}{\sqrt{\pi}}\sqrt{\frac{m_j}{2T_{||j}(x)}}\exp\left[-\frac{m_j(v_{||j}(x)-U_{||j}(x))^2}{2T_{||j}(x)}\right],$$
$$f_{0\perp j}=\frac{1}{\pi}\frac{m_jn_j(x)}{2T_{\perp j}(x)}\exp\left[-\frac{m_j(v_{\perp j}(x)U_{\perp j}(x))^2}{2T_{\perp j}(x)}-\frac{e_j\phi(x)}{\langle T\rangle}\right], \tag{3.2}$$

where $j=i,e$, $T_{||j}(x)$ and $T_{\perp j}(x)$ are the parallel and perpendicular temperature, $U_\perp(x)$ and $U_{||}(x)$ are the mean velocity in the perpendicular and parallel directions $\phi(x)$ is the self-consistent electric potential, $\langle T\rangle$ is the local averaged temperature, and m_j, n_j are particle mass and density. (Here r is expanded around r_0 with respect to gyro-radius and a new coordinate x given by $x=r-r_0+v_{\theta j}+\Omega_j$ is used.)

Taking the 0-th to the second moments of Eq. (3.1), we obtain

$$m_j\left[\frac{\partial n_j}{\partial t}+\nabla\cdot(\boldsymbol{\Gamma}_j)\right]=-\frac{\partial}{\partial x}\Gamma^M_{xj} \tag{3.3}$$

$$m_jn_j\left(\frac{\partial \boldsymbol{U}_j}{\partial t}+\boldsymbol{U}_j\cdot\nabla\boldsymbol{U}_j\right)-\frac{e_j}{c}\boldsymbol{\Gamma}_j\times\boldsymbol{B}+\nabla\cdot p_j$$
$$=-\frac{\partial}{\partial x}\boldsymbol{P}^M_{xj}+[n_je_j\boldsymbol{E}-\nabla\cdot(\mathbf{P}_j-p_j\mathbf{I})] \tag{3.4}$$

$$\frac{\partial}{\partial t}(3p_j)+\nabla\cdot\boldsymbol{Q}_j+2\mathbf{P}_j:\nabla\boldsymbol{U}_j$$
$$=-\frac{\partial}{\partial x}Q^M_{xj}+e_j(\boldsymbol{\Gamma}_j-n_j\boldsymbol{U}_j)\cdot\boldsymbol{E} \tag{3.5}$$

for each particle species. $\boldsymbol{\Gamma}_j=n_j\boldsymbol{U}_j$, represents the particle flux defined by $\boldsymbol{\Gamma}_j=\int \boldsymbol{v}f_jd^3v$, $n_j=\int f_jd^3v$ is the density, $p_j=n_jT_j$ $(\equiv\int m_j(\boldsymbol{v}_j-\boldsymbol{U}_j)^2f_jd^3v)$ is the pressure, $\boldsymbol{U}_j$ is the mean velocity, and $\boldsymbol{Q}_j=3T_j\boldsymbol{\Gamma}_j+\boldsymbol{q}_j$ is the heat flux, where

$$\boldsymbol{q}_j=\int m_j(\boldsymbol{v}_j-\boldsymbol{U}_j)|\boldsymbol{v}_j-\boldsymbol{U}_j|^2f_jd^3v \tag{3.6}$$

is the heat conduction, $\mathbf{P}_j$ is the stress tensor and $\mathbf{I}$ is a unit tensor. In this study $U_{||j}$ and $U_{\perp j}$ are considered as the mean velocity. Terms Γ^M_{xj}, P^M_{xj} and Q^M_{xj} are the particle, momentum and heat fluxes induced by the magnetic stochasticity where the subscript x stands for the direction which is perpendicular to the mean magnetic field line. They are given by

$$\Gamma^M_{xj}\equiv-\int|v_{||j}|D_M\frac{\partial f_{0j}}{\partial x}d^3v_j\ , \tag{3.7}$$

$$P^M_{||xj}\equiv-\int|v_{||j}|m_j(v_{||j}-U_{||j})D_M\frac{\partial f_{0j}}{\partial x}d^3v_j\ , \tag{3.8}$$

$$P^M_{\perp xj}\equiv-\int|v_{||j}|m_j(v_{\perp j}-U_{\perp j})D_M\frac{\partial f_{0j}}{\partial x}d^3v_j\ , \tag{3.9}$$

$$Q^M_{xj}\equiv-\int|v_{||j}|\frac{1}{2}m_j(v_{||j}-U_{||j})^2D_M\frac{\partial f_{0j}}{\partial x}d^3v_j\ , \tag{3.10}$$

In order to calculate the above fluxes, the integrals of

$$\frac{1}{v_{T||}{}^{m+1}}\int_{-\infty}^{\infty}|v_{||}|(v_{||}-U_{||}(x))^mf_{0||}dv_{||}\ , \tag{3.11}$$

$$\frac{1}{v_{T\perp}{}^{m+1}}\int_{-\infty}^{\infty}|v_{\perp}|(v_{\perp}-U_{\perp}(x))^mf_{0\perp}dv_{\perp}\ , \tag{3.12}$$

for $m=0$, 1, 2, 3 and 4 are needed. In performing the integration the thermodynamic forces are defined as

$$X_{1j}=\frac{1}{n_j}\frac{dn_j}{dx}-\frac{1}{2}\frac{1}{T_j}\frac{dT_j}{dx}+\frac{e_j}{\langle T\rangle}\frac{d\phi}{dx}\ , \tag{3.13}$$

$$X_{2j}=\frac{2}{v_{Tj}}\frac{dU_{\|j}(x)}{dx}\ , \tag{3.14}$$

$$X_{3j}=\frac{2}{v_{Tj}}\frac{dU_{\perp j}}{dx}\ , \tag{3.15}$$

$$X_{4j}=\frac{1}{T_j}\frac{dT_j}{dx}\ , \tag{3.16}$$

where $v_{Ti}\equiv\sqrt{2T_j/m_j}$ is thermal velocity, for $T_j\equiv T_{\|j}=T_{\perp j}$. Introducing normalized quantities given by,

$$\hat{\Gamma}^M_{xj}=\frac{\Gamma^M_{xj}}{n_j v_{Tj}}\ ,\ \hat{P}^M_{\|xj}=\frac{P^M_{\|xj}}{n_j m_j v_{Tj}}\ ,\ \hat{P}^M_{\perp xj}=\frac{P^M_{\perp xj}}{n_j m_j v_{Tj}}\ ,$$

$$\hat{Q}^M_{xj}=\frac{Q^M_{xj}}{n_j v_{Tj} T_j}\ .$$

The thermodynamic forces-fluxes relation is obtained as

$$\begin{pmatrix}\hat{\Gamma}^M_{xj}\\ \hat{P}^M_{\|xj}\\ \hat{P}^M_{\perp xj}\\ \hat{Q}^M_{xj}\end{pmatrix}=-\frac{1}{\pi}D_M\exp\left[-\frac{e_j\phi(x)}{\langle T\rangle}\right]\times\begin{pmatrix}K_0 & K_1 & 0 & K_3\\ K_1 & K_2 & 0 & K_4\\ 0 & 0 & K_5 & 0\\ K_3 & K_4 & 0 & K_6\end{pmatrix}\begin{pmatrix}X_{1j}\\ X_{2j}\\ X_{3j}\\ X_{4j}\end{pmatrix} \tag{3.17}$$

The matrix elements K_0, K_1, K_2, K_3, K_4, K_5, K_6 are expressed as

$$K_0=\frac{1}{\sqrt{\pi}}e^{-X_{0j}^2}+_{0j}\{1-2\Phi(\sqrt{2}X_{0j})\}, \tag{3.18}$$

$$K_1=\Phi(\sqrt{2}X_{0j})-\frac{1}{2}\ , \tag{3.19}$$

$$K_2=\frac{1}{\sqrt{\pi}}e^{-X_{0j}^2}+X_{0j}\left\{\Phi(\sqrt{2}X_{0j})-\frac{1}{2}\right\}, \tag{3.20}$$

$$K_3=\frac{1}{\sqrt{\pi}}e^{-X_{0j}^2}+X_{0j}\left\{\Phi(\sqrt{2}X_{0j})-\frac{1}{2}\right\}, \tag{3.21}$$

$$K_4=\frac{1}{2\sqrt{\pi}}X_{0j}e^{-X_{0j}^2}+\frac{3}{2}\left\{\Phi(\sqrt{2}X_{0j})-\frac{1}{2}\right\}, \tag{3.22}$$

$$K_5=\frac{1}{\sqrt{\pi}}e^{-X_{0j}^2}+X_{0j}\{1-2\Phi(\sqrt{2}X_{0j})\}, \tag{3.23}$$

$$K_6=\frac{1}{2\sqrt{\pi}}X_{0j}^2e^{-X_{0j}^2}+\frac{2}{\sqrt{\pi}}e^{-X_{0j}^2}+\frac{3}{2}\left\{\Phi(\sqrt{2}X_{0j})-\frac{1}{2}\right\}X_{0j}\ , \tag{3.24}$$

where $X_{0j}\equiv U_{\|j}(x)/v_{Tj}$ and $\Phi(x)$ is the error function defined by

$$\Phi(x)=\frac{1}{\sqrt{2\pi}}\int_{-\infty}^{x}e^{-t^2/2}dt\ .$$

Taking the limit that where X_{0j} is small compared to unity, the error function, $\Phi(X_{0j})$ is expanded with respect to X_{0j} and the terms up to the 2nd order of X_{0j} are retained. In this case, the thermodynamic forces-fluxes relation reduces as

$$\begin{pmatrix}\hat{\Gamma}^M_{xj}\\ \hat{P}^M_{\|xj}\\ \hat{P}^M_{\perp xj}\\ \hat{Q}^M_{xj}\end{pmatrix}=-\frac{1}{\pi}D_M\exp\left[-\frac{e_j\phi(x)}{\langle T\rangle}\right]\times\begin{pmatrix}1+X_{0j}^2/2 & X_{0j} & 0 & 1\\ X_{0j} & 1 & 0 & X_{0j}\\ 0 & 0 & 1+X_{0j}^2/2 & 0\\ 1 & X_{0j} & 0 & 2\end{pmatrix}\begin{pmatrix}X_{1j}\\ X_{2j}\\ X_{3j}\\ X_{4j}\end{pmatrix}, \tag{3.25}$$

where the determinant of the matrix up to the 2nd order of X_{0j} is given to be 1. The alternative orthogonal relation between fluxes and forces could be chosen in Eqs. (3.17) and (3.25). However, here we adopt Eq. (3.25) to consider the following transport process.

3.3 Application of the transport matrix

3.3.1 Electric field on the multifold structure of the magnetic field

Using the obtained matrix (3.17), we study the generation of electric field in the stochastic region. In this region, the thermal velocity of electron is larger than that of ion, so that the electron flux is greater than the ion flux. The transport in this region is intrinsically bipolar and the electric field can be induced. The electric potential in the distribution function in

Eq. (3.2) is introduced so as to be consistent with this electric field.

We assume the model magnetic field structure, shown in Fig. 3.1, where the stochastic region is put between the non-stochastic regions. (In the non-stochastic region, we assume that magnetic field lines form the magnetic surfaces.) The particles flux and heat flux flow across each region along the x direction. The non-stochastic regions are labeled as 1, 3, and the stocahstic region as 2. The region 2 is assumed to be thin so that the slab geometry can be used.

In order to study the electric field formation in the stochastic region, the boundary conditions on the surface between regions 1 and 2 as well as between regions 2 and 3 are necessary. A static case is considered and the condition that the particle and heat fluxes across the boundaries are continuous is imposed. To this end the transport matrix in the non-stochastic regions (1, 3 regions) is assumed to be given as

$$\begin{pmatrix} \hat{\Gamma}_{xj}^{(1,3)} \\ \hat{P}_{\|xj}^{(1,3)} \\ \hat{P}_{\perp xj}^{(1,3)} \\ \hat{Q}_{xj}^{(1,3)} \end{pmatrix} = - \begin{pmatrix} \overline{D}_j & 0 & 0 & 0 \\ 0 & \overline{\mu}_{\|j} & 0 & 0 \\ 0 & 0 & \overline{\mu}_{\perp j} & 0 \\ 0 & 0 & 0 & \overline{\chi}_j \end{pmatrix} \begin{pmatrix} X_{1j}^{(1,3)} \\ X_{2j}^{(1,3)} \\ X_{3j}^{(1,3)} \\ X_{4j}^{(1,3)} \end{pmatrix} \tag{3.26}$$

where $\overline{D}_j$, $\overline{\mu}_j$ and $\overline{X}_j$ are the effective diffusivity, viscosity and heat conductivity, respectively. Here we consider the case where the transport mechanisms in region 1 and in region 3 are the same and hence use the same transport matrix. The matrix in the stochastic region (region 2) is given by Eq. (3.25), and it is assumed that the mean particle velocity is small enough compared with the thermal velocity, that is $X_{0j} \simeq 0$. We use the superscripts (1, 3) and (2) for distinguishing the regions.

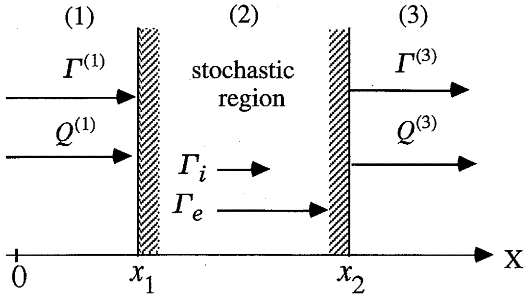

Fig. 3.1 The model plasma structure. The x axis is in the minor radius direction. The regions (1) and (3) are the magnetically non-stochastic regions, and region (2) is the stochastic region. The particle flux and energy flux flow in the x direction.

The corresponding thermodynamic forces are

$$X_{1j}^{(k)} = \kappa^{(k)} - \frac{1}{2}\kappa_{T_j}^{(k)} + \frac{e_j}{\langle T \rangle} E^{(k)}, \tag{3.27}$$

$$X_{4j}^{(k)} = \kappa_{T_j}^{(k)}, \tag{3.28}$$

$$\kappa^{(k)} = \frac{1}{n^{(k)}} \frac{dn^{(k)}}{dx}, \tag{3.29}$$

$$\kappa_{T_j}^{(k)} = \frac{1}{T_j^{(k)}} \frac{dT_j^{(k)}}{dx} \tag{3.30}$$

where $(k) = (1, 3)$ or (2).

The continuity conditions of the particle and heat fluxes across the boundaries are given by

$$\Gamma_e^{(1)} = \Gamma_e^{(2)} = \Gamma_e^{(3)}, \tag{3.31}$$

$$\hat{Q}_j^{(1)} = \hat{Q}_j^{(2)} = \hat{Q}_j^{(3)}. \tag{3.32}$$

Ion and electron particle fluxes are constrained by thea mbipolar condition in each region as,

$$\Gamma_e^{(1)} = \Gamma_i^{(1)},\ \Gamma_e^{(2)} = \Gamma_i^{(2)},\ \Gamma_e^{(3)} = \Gamma_i^{(3)}. \tag{3.33}$$

Imposing these conditions, we calculate the electric field in each region, which can be written as

$$E^{(1,3)} = \frac{\langle T \rangle}{e(\overline{D}_i + \overline{D}_e)} \times \left[-\kappa^{(1,3)} (\overline{D}_e - \overline{D}_i) + \frac{1}{2} (\overline{D}_e \kappa_{Te}^{(1,3)} - \overline{D}_i \kappa_{Ti}^{(1,3)}) \right], \tag{3.34}$$

$$E^{(2)} = - \frac{\langle T \rangle}{4ea} [\overline{\chi}_e \kappa_{Te}^{(1,3)} - \overline{\chi}_i \kappa_i^{(1,3)}], \tag{3.35}$$

where

$$a \equiv \frac{1}{\pi} D_M \exp\left[- \frac{e\phi(x)}{\langle T \rangle} \right]. \tag{3.36}$$

For convenience the electron diffusivity is taken to be the same as the ion diffusivity in regions 1 and 3, that is $\overline{D}_e = \overline{D}_i$. Then the Eq. (3.34) can be rewritten as

$$E^{(1,3)}=\frac{\langle T\rangle}{4e}[(\kappa_{Te}^{(1,3)}-\kappa_{Ti}^{(1,3)})] \tag{3.37}$$

The electric field in region 2, $E(2)$ should be written as $E(2)=-d\phi/dx$ in the consistent manner. Then Eq. (3.35) is re-written as

$$\frac{d}{dx}\left\{\exp\left[-\frac{e\phi(x)}{\langle T\rangle}\right]\right\}=\frac{\pi}{4D_M}\{\bar{\chi}_e\kappa_{Te}^{(1,3)}-\bar{\chi}_i\kappa_{Ti}^{(1,3)}\}$$
$$=\frac{\pi}{4D_M}\left\{\frac{q_e}{v_{Te}T_e}-\frac{q_i}{v_iT_i}\right\}, \tag{3.38}$$

where q_e and q_i are the x-components of heat flux given by Eq. (3.6). The right hand side of Eq. (3.38) is evaluated by the quantities at the boundary. The general solution of the potential in the region 2 is obtained as

$$-\frac{e\phi(x)}{\langle T\rangle}$$
$$=\ln\left[\frac{\pi}{4D_M}\left\{\frac{q_e}{v_{Te}T_e}-\frac{q_i}{v_{Ti}T_i}\right\}(x-x_1)+exp\left\{-\frac{e\phi(x_1)}{\langle T\rangle}\right\}\right], \tag{3.39}$$

where $\phi(x_1)$ is the potential at $x=x_1$. Differentiating Eq. (3.39), the normalized field is given by

$$-\frac{e}{\langle T\rangle}\frac{d\phi(x)}{dx}$$
$$=\frac{\frac{\pi}{4D_M}\left[\frac{q_e}{v_{Te}T_e}-\frac{q_i}{v_{Ti}T_i}\right]}{\frac{\pi}{4D_M}\left[\frac{q_e}{v_{Te}T_e}-\frac{q_i}{v_{Ti}T_i}\right](x-x_1)+exp\left\{-\frac{e\phi(x_1)}{\langle T\rangle}\right\}}, \tag{3.40}$$

This electric field has hyperbolic dependence on x. We can see from Eq. (3.40) that the electric field in the stochastic region, region 2, depends on the difference of the thermal mobility ratio between ion's and electron's heat fluxes, $q_i/(D_Mv_{Tj}T_j)$, in the adjoined non-stochastic regions.

Next using the transport matrix, Eq. (3.25), and a modeled plasma configuration shown in Fig. 3.1, we consider the temperature distribution in the stochastic region. We impose the stationary condition and assume that the heat fluxes are constant as $q_{0j}\equiv q_j^{(1)}(x)=q_j^{(2)}(x)=q_j^{(3)}(x)$, where the $q_j^{(k)}(x)$ is the heat flux, and consider the case where $qe\gg qi$. The electron heat flux in the regions 1, 3 is described by

$$q_e^{(1,3)}(x)=-\bar{\chi}_{0e}\frac{d}{dx}T_e^{(1,3)}(x). \tag{3.41}$$

The electron heat flux in the stochastic region is described by

$$\frac{q_e^{(2)}(x)}{v_{Te}T_e^{(2)}(x)}=-\frac{D_M}{\pi}\left[-\frac{e\phi(x)}{\pi}\right]$$
$$\left(\frac{3}{2}\frac{1}{T_e^{(2)}(x)}\frac{\partial T_e^{(2)}(x)}{\partial x}+\frac{e}{\langle T\rangle}\frac{d}{dx}\phi(x)\right), \tag{3.42}$$

if we approximate as $\kappa(k)\simeq 0$. Combining Eq. (3.39) with Eqs. (3.41) and (3.42), we obtain the temperature distribution in each region as

$$T_e^{(1)}(x)=-\frac{q_{0e}}{\bar{\chi}_{0e}}x+T_{0e},$$
$$T_e^{(3)}(x)=-\frac{q_{0e}}{\bar{\chi}_{0e}}(x-x_2)+T_{2e}, \tag{3.43}$$

$$T_e^{(2)}(x)=\left(\frac{\frac{\pi\sqrt{m_e}}{\sqrt{2}D_M}q_{0e}(x-x_1)+T_{1e}^{3/2}\exp\left\{-\frac{e\phi(x_1)}{\langle T\rangle}\right\}}{\frac{\pi}{4D_M}\left[\frac{q_{0e}}{v_{Te}T_{1e}}-\frac{q_{0i}}{v_{Ti}T_{1i}}\right](x-x_1)+\exp\left\{-\frac{e\phi(x_1)}{\langle T\rangle}\right\}}\right)^{2/3}, \tag{3.44}$$

where $\bar{\chi}_{0e}$ is chosen to be constant, $T_{0e}=T_e^{(1)}(0)$, $T_{1e}=T_e^{(1)}(x_1)$ and $T_{2e}=T_e^{(2)}(x_2)$.

Using Eqs. (3.39), (3.43) and (3.44), we calculate the electric field and the temperature distribution for the parameters of a tokamak plasma, the major radius $R0=3m$, the minor radius $a=1m$, $T_0=1keV$, $\bar{\chi}_{0e}=10m^2/s$. The value of the diffusivity of the magnetic field line D_M is that, $D_M=(\delta r)^2/2\pi R_0=5\times10^{-5}m$, $\delta r=2.5\times10^{-2}m$ or $\tilde{B}/B=10^{-3}$ which is estimated by the Chirikov condition. Normalizations are given as $E(2)=E(2)/(\langle T\rangle a/e)$ and $x=x/a$. The results are shown in Fig. 3.2 for $q_{0e}=10keVm/s$, where $q_{0j}\ll q_{0j}$ is assumed. The temperature distribution in the sotchastic region becomes flat and the positive radial electric field is formed in the stochastic region 2.

3.3.2 Effect of the $E\times B$ drift

In this subsection, we consider the effect of the $E\times B$ drift to the transport. The transport in the stochastic region in intrinsically bipolar and the electric field can be induced. The case with $X_{0j}=0$ is considered for simplicity. The slab geometry with the non-stochastic region inside the stochastic region outside is considered. The interface is denoted by $x=0$.

The $\boldsymbol{E}\times\boldsymbol{B}$ drift occurs due to the ambipolar electric field and this drift causes the flow of the perpendicular momentum in the x direction, $P^M_{\perp xj}$, if the velocity gradient exists. The motion is dominated by the ion, therefore we consider the ion momentum flux $P^M_{\perp xi}$. The $E\times B$ drift

$$U_{\perp i}(x) = -\frac{E}{B} = \frac{d\phi(x)}{dx}\frac{1}{B} \tag{3.45}$$

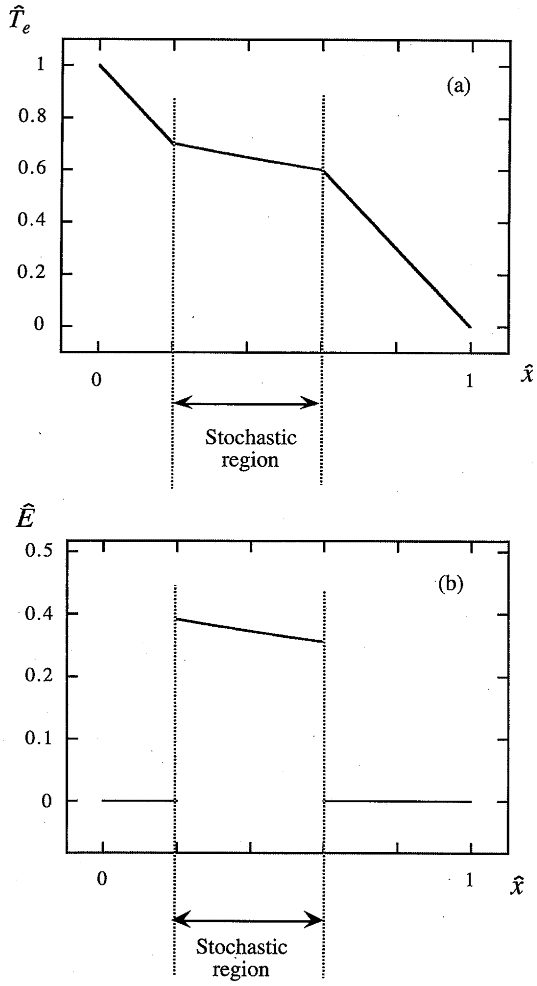

Fig. 3.2 (a) The temperature distribution. (b) The induced electric field distribution. $\hat{T}$, $\hat{E}$ and $\hat{x}$ are the normalized temperature, normalized electric field and normalized minor radius. The stochastic region is bounded by $\hat{x}=0.2$ and $\hat{x}=0.6$.

is considered as a perpendicular ion velocity and higher order velocity such as ion polarization velocity is neglected. Substituting this relation into Eq. (3.25), we obtain the momentum flux as

$$P^M_{\perp xi} = -\frac{D_M}{\sqrt{\pi}\, eB} m_i n(x) \exp[-\hat{\phi}(x)]\langle T\rangle \frac{d^2\phi(x)}{dx^2}, \tag{3.46}$$

where $\hat{\phi}(x)$ is the normalized electric potential as $\hat{\phi}(x) = e\hat{\phi}(x)/\langle T\rangle$.

The direction of flux is shown in Fig.3.3. This equation is rewritten as

$$\frac{d^2\hat{\phi}(x)}{dx^2} = -\frac{\sqrt{\pi}\, P^M_{\perp xi} eB}{D_M m_i n(x)\langle T\rangle} \exp[\hat{\phi}(x)] . \tag{3.47}$$

For a given constant $P^M_{\perp xj}$, the characteristic width of this electric potential is estimated as

$$d = \sqrt{\frac{D_M m_i n(x)\langle T\rangle}{\sqrt{\pi}\, P^M_{\perp xi} eB}} . \tag{3.48}$$

To calculate the electric field, we use the ambipolar condition as $\Gamma^M_{xe} = \Gamma^M_{xi}$ or $n v_{Te}\Gamma^M_{xe} = n v_{Ti}\Gamma^M_{xi}$. The electron thermal velocity is greater than that of ion ($v_{Te} \gg v_{Ti}$), so that the ambipolar condition is approximated as $\Gamma^M_{xe} \simeq 0$ or,

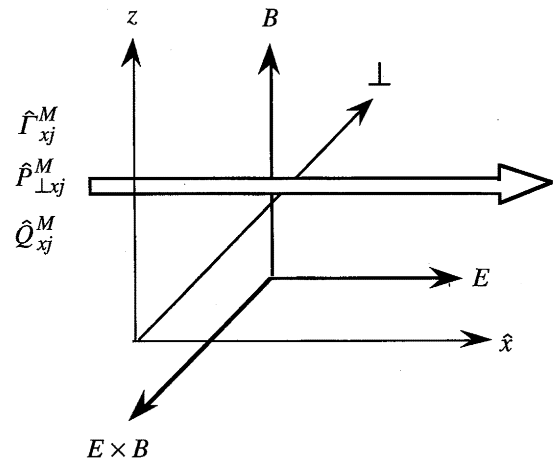

Fig. 3.3 The coordinate system used in the transport matrix. x and z xis are taken along the minor radius and toroidal direction, respectively. B is the mean magnetic field and E is the electric field generated by the ambipolar condition. The direction of the $E\times B$ drift is also shown.

$$\frac{1}{n(x)}\frac{dn(x)}{dx}+\frac{1}{2}\frac{1}{T_e(x)}\frac{dT_e(x)}{dx}-\frac{d}{dx}[\hat{\phi}(x)]=0\,. \tag{3.49}$$

The electron heat flux is only calculated, since the electron heat transport is much greater than the ion heat transport. The electron heat flux is rewritten from Eq. (3.25) as

$$Q^M_{xe}=$$
$$-D_M\frac{n(x)}{\sqrt{\pi}}T_e(x)\sqrt{\frac{2T_e(x)}{m_e}}\exp[\hat{\phi}(x)]\frac{1}{T_e(x)}\frac{dT_e(x)}{dx}, \tag{3.50}$$

where Q^M_{xe} is assumed to be constant. Combining the Eqs. (3.47), (3.49) and (3.50), we obtain the profiles of the density, the temperature and the electric field. Let us consider the stationary case. The particles, heat and momentum fluxes are constant and continuous across the boundary. The density, the temperature and the electric field are normalized as $\hat{n}(x)=n(x)/n_0$, $\hat{T}_e(x)=T_e(x)/T_{e0}$ and $\hat{E}(x)=E(x)/(\langle T\rangle r_s/e)$, where rs is the characteristic width of the stochastic region, n_0 and T_{e0} are the density and the temperature at the boundary between the stochastic region and the non-stochastic region at the core side, respectively. The boundary conditions are that $\hat{n}(0)=1$, $\hat{T}_e(0)=1$, $\hat{E}(0)=0$ and $\hat{\phi}(0)=0$ and $Q^M_{xe}=q_{e0}$, where q_{e0} is estimated as $q_{e0}=n_0\times 5keVm/s$ by using typical plasma parameters and $D_M=1.0\times10^{-5}m$ and $P^M_{\perp xi}=n_0m_i\times2.0\times10^{-4}m/s$ are used in this calculation.

The profiles of $\hat{n}$, $\hat{T}_e$, $\hat{E}$ and $\hat{\phi}$ in the stochastic region are shown in Fig.3.4. The density decreases in the region of $0<\hat{x}<0.6$ and increases rapidly for $\hat{x}>0.6$ (Fig.3.4 (a)), while the temperature profile is flat in the region of $0<\hat{x}<0.75$ and decreases rapidly for $\hat{x}<0.75$ (Fig.3.4 (b)). The electric field grows lineally for $0<\hat{x}<0.6$ and becomes flat for $\hat{x}>0.6$ (Fig. 3.4 (c)). The electric field indicates the ion sheath whose width is about 0.6. This value is consistent with the rough estimate of d, $d=0.17m$ ($d/r_s\simeq0.57$), from Eq. (3.48). The mean temperature $0\leq x\leq0.8$ is $\langle T_e\rangle/T_{e0}=0.91$.

We see from Fig.3.4 that the electric field becomes flat for $\hat{x}>0.6$ and the velocity gradient becomes nearly zero, $dU_{\perp i}/d\hat{x}\simeq0$. $\hat{n}(x)$ increases to infinity in this region, to keep the constant momentum flux condition ($P^M_{\perp xi}$=const. in Eq. (3.47)). The electrons are trapped in the region $\hat{x}>0.6$ by the induced electric field by the ambipolar condition. This is seen in Fig.3.4 (a). The heat conductivity is decreased by the electric field and by the increase of the density for $\hat{x}>0.6$, since the heat flux is assumed to be constant.

3.4 Summary and discussion

In this chapter we formulated the plasma transport matrix in the stochastic magnetic field structure by use of the kinetic equation which included the ef-

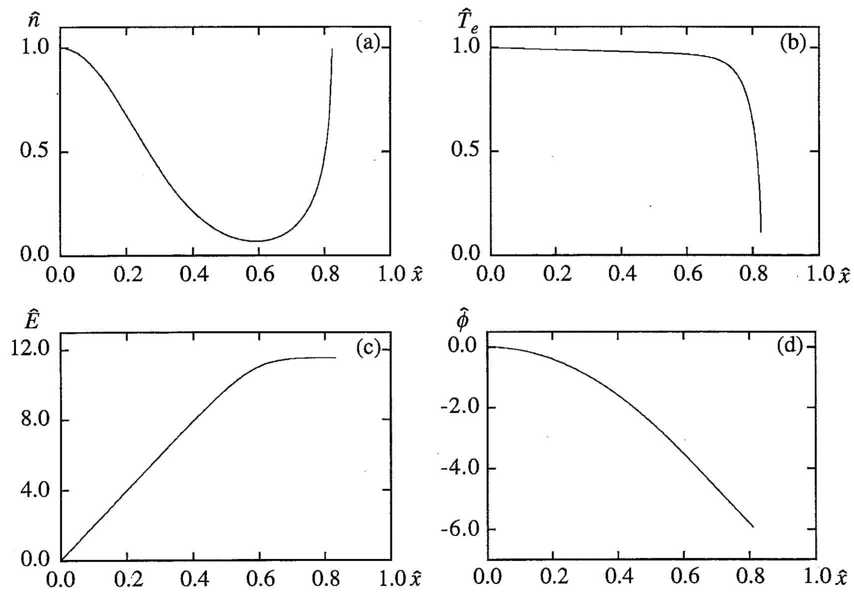

Fig. 3.4 The profiles of density (a), temperature (b), electric field (c) and electric potential (d). $\hat{n}$, $\hat{T}_e$, $\hat{E}$ and $\hat{\phi}$ versus $\hat{x}$ are shown, respectively.

fect of the magnetic stochasticity. In the calculation, we assumed that the distribution of plasma particles was shifted Maxwellian.

To apply the transport matrix, a simple study of the electric field generation and of the temperature distribution in the stochastic region was made. The electron flux was at most root-mass-ratio greater than that of ion, therefore the flux was bipolar and the electric field can be induced.

At first we applied the transport matrix to the modeled plasma configuration which had a layered structure in the radial direction (Fig.3.1). The case for $q_e \gg q_i$ was considered. We used the ambipolar condition for the particle flux in each region and the particle and the heat fluxes were continuous at the boundary between the stochastic and non-stochastic region. The electric field was generated due to the presence of stochastic magnetic diffusion and was formed in accordance with the heat conductivity and temperature gradient in the non-stochastic region. It had a hyperbolic dependence on x, if D_M, $\bar{\chi}_e$ and $\bar{\chi}_i$ were uniform. We also obtained the associated temperature distribution in the stochastic region by use of the transport matrix.

The generated electric field would induce the plasma motion. The flow was determined by the force from the electric field and the viscous drags in the stochastic/non-stochastic regions. Using Eqs. (3.4) and (3.5), we obtained the consistent electric field structure and the induced plasma flow. The ambipolar electric field caused the $E \times B$ drift. We introduced the thermodynamic force $dU_{\perp i}/dx$ and combined the equations of particle, momentum and heat fluxes. We obtained the stationary profiles of the density, the temperature and the electric field under the constant momentum and heat supply. When the momentum supply was large enough to make the characteristic width of the viscous ion sheath d be $d < r_s$, than a stationary solution of the density tends to be infinity and of the temperature tended to be zero at $\hat{x} > d$. Whether the finite static electric potential would be generated in the stochastic region under the boundary conditions with constant heat and momentum fluxes or not is not yet clear. This is left for our future work.

The electric field as well as the associated dissipation affects the global MHD mode stability itself. The stability and the fluctuation level determine the characteristics of the stochasticity, e.g., the width of the region, the magnitude of D_M and whether the global stochasticity sets in or not, etc., These effects should be examined to obtain the consistent solution.

Here we examined only the one dimensional model. The MHD perturbations in tokamaks, including the magnetic island, have helical structures. The formation of the stochastic region is associated with the helical perturbation and is essentially two dimensional. In order to develop a deeper understanding of electric field formation, two dimensional model should be considered. This is left for our future work.

4. 1-D simulation of sawtooth crash based on turbulence-turbulence transition model

We considered the anomalous transport in the static stochastic magnetic field and derived the transport matrix in the previous chapter. We obtained the static profiles of the density, the temperature and the ambipolar electric field using the transport matrix. However, the dynamics of the magnetic stochastization and the plasma transport are not analyzed. We, here, study the temporal evolution of the magnetic stochasticity and the dynamical behavior of the temperature collapse. The turbulence-turbulence transition model which is mentioned in subsection 2.2.3 is employed. The hysteresis characteristics of the heat conductivities are incorporated into the 1-dimensional transport code. The crash of the temperature profile and the propagation of the crash front (avalanche) are realized in this analysis.

4.1 Introduction

The sawtooth crash is a common feature of the ohmic and additionally heated plasma in the majority of tokamaks [2]~[4]. As described in section 2.1, theoretical models based on Kadomtsev's magnetic reconnection model are insufficient to explain the sawtooth crash. Recently, a turbulence-turbulence transition model between the L-mode and the M-mode has been proposed in order to explain the rapid crash of the temperature profile. This model has been applied to the 0-dimensional analysis of the thermal transport and the sawtooth-like oscillation has been obtained [20]. However, neither the propagation of a bifurcating point or the development of the temperature profile during the crash has not been analyzed.

In this chapter, we employ the 1-dimensional transport, including the hysteresis characteristics of the heat conductivity and analyze the temporal change of the spatial structure of temperature. The dynamics of the collapse are analyzed. The propagation of the crash front and the avalanche of the transition processes are studied. The oscillation of the pressure gradient is also examined.

This chapter is organized as follows. In section 4.2, the model of transport simulation is described. The simulation results with inclusion of the turbulence-turbulence transition model are given in section 4.3. The avalanche process is analyzed with respect to the threshold values of the transition. The time evolution of the pressure gradient is shown to understand the temperature collapse. The dependence of the oscillation period on the threshold value and the limitation of the crashed region are examined. Summary and discussion are given in section 4.4.

4.2 Simulation model

We introduce a simplified turbulence-turbulence transition model to analyze the temperature crash during the ohmic discharge. A sawtooth crash without precursor oscillations is considered. The transport model and the basic equations are shown.

4.2.1 Basic equations

In the numerical simulation, we employ the transport code TASK/TR [36] combined with the turbulence-turbulence transition model, in order to elucidate the mechanism of the heat transport. In this 1-dimensional transport code, a circular plasma cross section is assumed. We solve the developments of the plasma temperatures of electrons and ions T_e and T_i, and poloidal magnetic field B_p. The 1-dimensional radial transport equations are,

$$\frac{3}{2}\frac{\partial}{\partial t}(n_eT_e)=-\frac{1}{r}\frac{\partial}{\partial r}\left(r\chi_e\frac{\partial}{\partial r}n_eT_e\right)+P^e_{OH}-P_{eq}\ , \tag{4.1}$$

$$\frac{3}{2}\frac{\partial}{\partial t}(n_iT_i)=-\frac{1}{r}\frac{\partial}{\partial r}\left(r\chi_i\frac{\partial}{\partial r}n_iT_i\right)+P_{eq}\ , \tag{4.2}$$

$$\frac{\partial B_p}{\partial t}=\frac{\partial}{\partial r}\left\{\frac{\eta}{r}\frac{\partial}{\partial r}(rB_p)-J_{bs}\right\}, \tag{4.3}$$

$$J_z=\frac{1}{\mu_0}\frac{1}{r}\frac{\partial}{\partial r}(rB_p)\ , \tag{4.4}$$

where r is the direction of minor radius, P_{eq} is the ion-electron energy equipartition rate as,

$$P_{eq}=\frac{3}{2}n_e\frac{(T_e-T_i)}{\tau_{ie}}\ ,\ \tau_{ie}=\frac{(2\pi)^{\frac{1}{2}}3\pi m_i m_e^{-\frac{1}{2}}T_e^{\frac{3}{2}}}{n_i e^4 \ln\Lambda}\ , \tag{4.5}$$

P^e_{OH} is the ohmic heating power as,

$$P^e_{OH}=\eta^{NC}J_z^2\ , \tag{4.6}$$

where η^{NC} is the neoclassical resistivity, n_j and m_j are the density and mass,respectively. The neoclassical bootstrap current (a kind of the thermoelectric current) J_{bs} is introduced. The neoclassical formulae of J_{bs} and η^{NC} are employed according to [37].

We do not consider either the other heating power input or the power loss. In the present simulation, the quasi-neutrality condition ($n_e=n_i$) are assumed and the density profile is fixed in time to the following form,

$$n_j(r)=\{n_j(0)-n_j(a)\}[1-(r/a)^2]+n_j(a)\ , \tag{4.7}$$

where $j=i,e$ denotes the particle species.

4.2.2 Hysteresis characteristics of the heat conductivity

The characteristics of heat conductivity adopted in this turbulence-turbulence transition model is as follows. Both the ordinary heat conductivities (L-mode), χ^L_j, and the heat conductivities at the enhanced transport mode (M-mode), χ^M_j, are assumed to be constant and independent of other parameters. The electron heat conductivity in the M-mode is assumed as

$$\chi^M_e=C_M\chi^L_e\ , \tag{4.8}$$

where C_M is taken to be a numerical constant. In the M-mode, the electron heat conductivity could be greater than that of ion's by the square root mass ratio, $\sqrt{m_i/m_e}$, therefore the ion heat conductivity is assumed as

$$\chi^M_i=(\chi^M_e-\chi^L_e)\cdot\sqrt{m_e/m_i}+\chi^L_i\ . \tag{4.9}$$

The pressure gradient is increased by the ohmic heating. When it exceeds the threshold value, the transition from the L-mode to the M-mode occurs and the heat conductivities are much enhanced compared with those in the L-mode. The normalized pressure gradient is expressed as, $\alpha=-q^2Rd\beta/d_r$, where q is the safety factor, $q=rB_T/RB_p$ and β is the ratio of the plasma pressure to the magnetic field pressure, $\beta=n(T_e+T_i)/(B^2/2\mu_0)$. The threshold value of α from the L-mode to the M-mode is given by α_c. Once the M-mode occurs, the pressure gradient is decreased by the enhanced heat transport. When α is reduced to the lower threshold value $\alpha_1(\alpha_1<\alpha_c)$, the back-transition from the M-mode to the L-mode occurs. We assume that the threshold values α_c and α_1 are given as external and free parameters. Figure 4.1 illustrates the model hysteresis curve for the heat conductivities. Using this model, we analyze the plasma thermal transport with respect to the changes of C_M, α_c and α_1. These parameters have been estimated in subsection 2.2.3, however we here assume that they are free parameters, and analyze the dependence of the heat transport on their variations. We also assume that the transport bifurcation occurs inside the $q=1$ surface.

The heat conductivities adopted in this turbulence-turbulence transition model (Eqs. (4.1) and (4.2)) are given as,

$$\chi_j=\begin{cases}\chi_j^L+\chi_j^{NC} & \text{(for the L-modo)}\\ \chi_j^M+\chi_j^{NC} & \text{(for the M-modo)}\end{cases}, \tag{4.10}$$

where χ_j^{NC} is the neoclassical heat conductivity. The neoclassical formula of χ_j^{NC} is also employed according to [37].

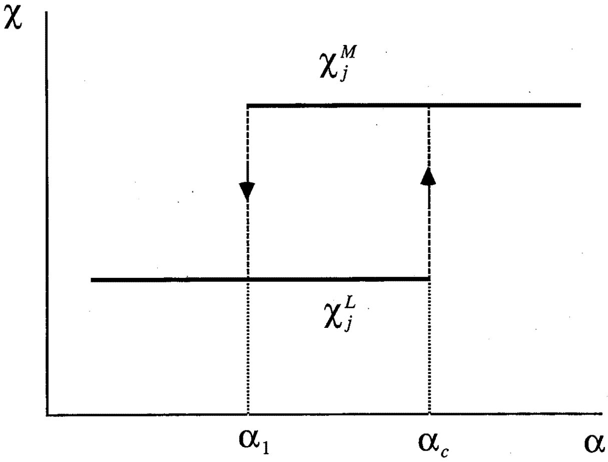

Fig. 4.1 The model hysteresis curve for the heat conductivity. χ_j^L and χ_j^M are the heat conductivities of the L-mode and the M-mode, respectively. α_c and α_1 are the threshold values of the transition and back-transition.

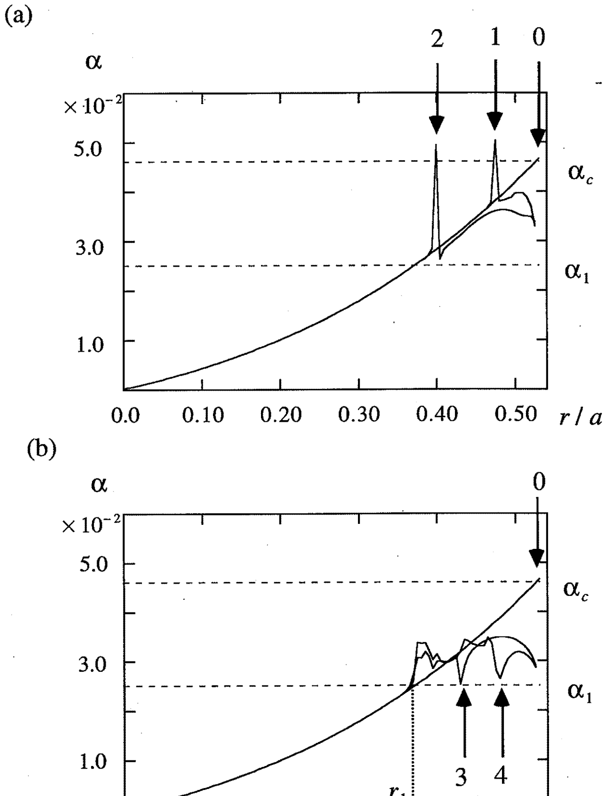

Fig. 4.2 The radial profile of the pressure gradient, α, inside the $q=1$ surface, where $q=1$ surface is located at $r/a=0.53$, is shown. The threshold values used for this case are $\alpha_c=4.65\times10^{-2}$ and $\alpha_1=2.50\times10^{-2}$. The horizontal axis is taken along the minor radius, r/a. The transitions from the L-mode to the M-mode (a) and the back-transition from the M-mode to the L-mode (b) are shown. The numbers $0\sim4$ indicate the time $t/\tau_{Ap}=0.0$, 1.1, 5.6, 8.9, 13.3, respectively.

4.3 Temporal evolution of temperature and collapse dynamics

Numerical simulation of the energy transport equations (Eqs. (4.1) ~ (4.10)) is done and the results are shown in this section. We choose the standard medium size tokamak parameters as : major radius R=1.3m, minor radius $a=3.5\times10^{-1}$m, the main magnetic field B_T=1.3T, the total plasma current $I_p=3.0\times10^{-1}$MA and the central density $n_j(0)=3.0\times10^{19}\mathrm{m}^{-3}$.

4.3.1 The propagation of the crash front

We first show the particular behavior of the temperature profile induced by the bifurcation of the heat conductivities. Figure 4.2 shows the time slices of the profile of the pressure gradient $\alpha(r)$ depicted from the transport simulation. The radial profiles of α inside the $q=1$ surface $(q<1)$ are plotted in Fig.4.2. The location of $q=1$ surface is $r/a=0.53$. We choose the threshold parameters as, $\alpha_c=4.65\times10^{-2}$, $\alpha_1=2.50\times10^{-2}$, where the value of α_c is adopted from the saturated value of the pressure gradient at the $q=1$ surface under the ohmic heating.

The successive transitions from the L-mode to the M-mode are shown in Fig.4.2 (a). The transition from the L-mode to the M-mode takes place at the $q=1$ surface when the pressure gradient, α, exceeds α_c, that is shown in the curve labeled No.0. The heat flux in the M-mode region is enhanced due to the large heat conductivities, χ_j^M, and the pressure gradient α in this region decreases. At the region adjacent to the M-mode region, the pressure gradient α is forced to increase due to the enhanced heat flux from the M-mode region. When the value of α exceeds α_c, another transition from the L-mode to the M-mode occurs. The curve labeled No.1 shows the profile of a after the time of $t/\tau_{Ap}=1.1$, where t denotes the time from the start of the transition process and $\tau_{Ap}(=a\sqrt{\mu_0 n m_i}/B_p)$ is the poloidal Alfvén time. In the region between $q=1$ surface and the surface where the value of a is peaked, the heat conductivities change from χ_j^L to χ_j^M and the flattening of the temperature profile is seen.

We see that the crash front propagates. As time goes on, the peaked point of α, which corresponds to the crash front, propagates inward from the surface labeled No.1 and reaches the peaked point labeled No.2 at $t/\tau_{Ap}=5.6$ (Fig.4.2 (a)). The propagation of the peak of α implies that the M-mode region spreads from the first transition point to the peaked point of α. In this region, α decreases due to the enhanced heat flux. We regard the propagation of the crash front as an avalanche.

When a decreases to α_1, the back-transition from the M-mode to the L-mode occurs. The time slice of a profile during the back-transition is shown in Fig.4.2 (b). The back-transition starts to occur in the vicinity of r_1, where $\alpha(r_1)=\alpha_1$, and propagates from r_1 to $q=1$ surface (labeled No.3 and 4) similar to the forward transition process. The labels of 1, 2 in Fig.4.2 (a) and 3, 4 in Fig.4.2 (b) correspond to the time at $t/\tau_{Ap}=1.1$, 5.6, 8.9 and 13.3, respectively.

The propagation of the forward transition (crash) and the back transition front is shown in Fig. 4.3, where the abscissa is the normalized radius, r/a, and the ordinate is taken as the normalized time, t/τ_{Ap}. The points marked with the ○ and × illustrate the propagation of the fronts for the different values of lower threshold value α_1; the cases of $\alpha_1=2.50\times10^{-2}$ (○) and $\alpha_1=2.70\times10^{-2}$ (×) are shown, respectively. The region of right hand side separated by the points

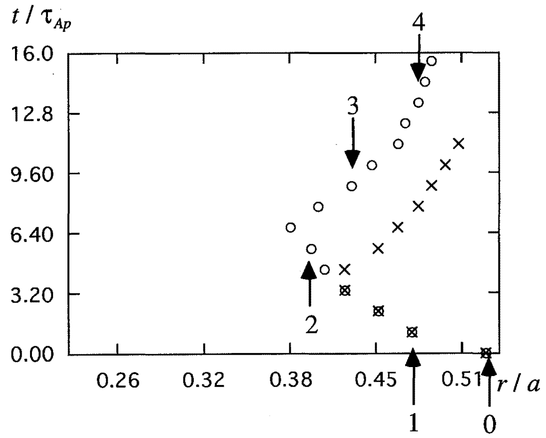

Fig. 4.3 The propagation of the crash fronts and their recovery are shown. The horizontal axis is r/a and vertical axis is t/τ_{Ap}. The ○ and × points show the cases of $\alpha_1=2.50\times10^{-2}$ and $\alpha_1=2.70\times10^{-2}$, respectively. Marked points indicate the location in time and real spae of the crash fronts. For the numbered points, the corresponding radial profiles of a are shown in Fig.2 indicated by the same numbers.

is considered to be the M-mode region. The numbers 0, 1, 2, 3 and 4 correspond to the numbered time slices with arrows shown in Fig.4.2. The numbers indicate the place of the transition front at the corresponding time. In the case of $\alpha_1=2.50\times10^{-2}$, the transition from the L-mode to the M-mode continues to about $t/\tau_{Ap}=6.4$, and after this time the back-transition, i.e., the transition from the M-mode to the L-mode, occurs. Comparing the two cases, we see that the crash front propagates deeper inside the plasma in accordance with the reduction of α_1. The forward propagation lines of crash fronts are seen to be almost straight as is shown in Fig.4.3. The velocity of the propagation of crash front, vcrash, is defined as the slope of this line. We find that the velocity of the forward propagation, v_{crash}, is independent of α_1, being nearly constant in time and of the order $v_{crash}\sim v_{Ap}\times 10^{-2}$. The crash time τ_{crash}, is defined as an interval between the starts of the crash and the starts of the recovering transition, that is $\tau_{crash}\sim 6.40\times\tau_{Ap}$ for the case of $\alpha=2.5\times10^{-2}$ and is of the order of $\tau_{crash}\sim\tau_{Ap}\times 10^1$. Note that the time needed for completing the back transition process is the similar order. This will be referred as the pulse length, τ_{pulse}, later.

The dependence of v_{crash} on the ratio of the heat conductivities $C_M(\equiv\chi_e^M/\chi_e^L)$, it is shown in Fig.4.4. The velocity, v_{crash}, is found to be proportional to C_M for the other fixed parameters. The crash time for given α_c and α_1 is inversely proportional to χ_e^M/χ_e^L.

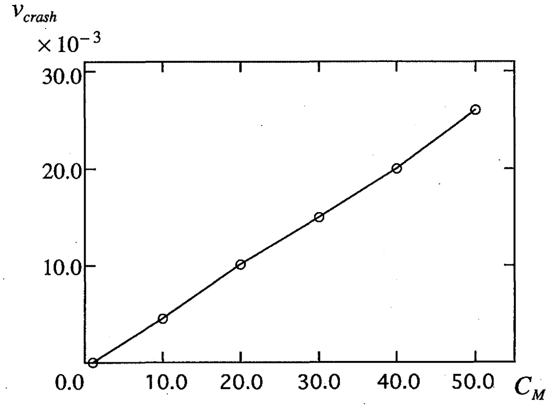

Fig. 4.4 The dependence of v_{crash} on the ratio of the heat conductivity of the M-mode to the L-mode heat conductivity, C_M, is shown.

4.3.2 The repetitive crashes of the temperature gradient

In this sub-section, we examine the oscillation of the temperature gradient as is revealed in the dynamic change of the pressure gradient. In the framework of our model, the periodic crash is realized by the repetition of the bifurcations of the heat conductivities. We attribute the sawteeth without precursor oscillation to this model.

The long time evolution of α is shown in Fig.4.5, its value at $r/a=0.52$, just inside the $q=1$ surface, is drawn. The time $t=0$ is set when the first crash occurs. The temporal evolution resembles the sawtooth oscillation, showing the rapid drop due to the enhanced heat flux and the slow increase by the ohmic heating. We see from Fig.4.5 that the period of the oscillation is order of $\tau_{saw}\sim\tau_{Ap}\times10^3$. For the fixed

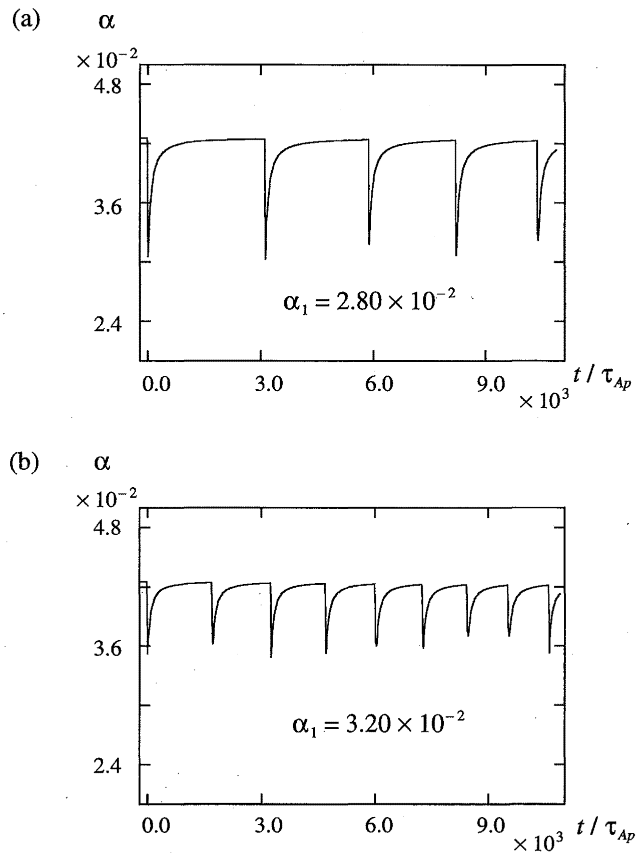

Fig. 4.5 The long time evolution of the pressure gradient, α. The horizontal axis is, t/τ_{Ap}. The changes of the value of α are observed at $r/a=0.52$. (a) $\alpha_1=2.80\times10^{-2}$ (B) $\alpha_1=3.20\times10^{-2}$

value of $\alpha_c=4.65\times10^{-2}$, the period depends on the α_1. The cases with different values of α_1 are compared in Fig.4.5(a) ($\alpha_1=2.80\times10^{-2}$) and (b) ($\alpha_1=3.20\times10^{2}$), respectively. Figure 4.6 shows the dependence of τ_{saw} on the value, $\alpha_c-\alpha_1$. The period is found to be proportional to $\alpha_c-\alpha_1$. It is clear that when $\alpha_c-\alpha_1\to0$, τ_{saw} approaches to zero.

The dynamic behavior of the associated heat flux is shown in Fig.4.7(a) and (b), they correspond to the cases of $\alpha_1=2.80\times10^{-2}$ and $\alpha_1=3.20\times10^{-2}$(Fig. 4.5(a) and (b)), respectively. We see that when the transition occurs, the heat pulses are induced. The normalized heat flux is defined as

$$\hat{q}_e(t)\equiv\frac{-\chi_e^{L,M}\nabla T_e(r_1,t)}{\chi_e^L\frac{T_e(0)}{a}}. \tag{4.11}$$

where r_1 is the observing point ($r_1/a=0.52$) and the superscript L or M denotes the heat conductivity at the L-mode or the M-mode. The heights of the heat pulse $\hat{q}_e$ are found to be regulated by α_c and χ_j^M. The values of $\hat{q}_e$ remain to be similar even if the value of α_1 differs. The bursting period, τ_{pulse}, (pulse length which was defined before) is the same order of the crash time.

The dependence of the long time energy outflow on the oscillation period, τ_{saw}, is shown in Fig.4.8. The outflow at $r_1/a=0.52$ is calculated, integrating over the interval between $t=t_0$ to $t=t_1$ ($t_0/\tau_{Ap}=0$ and $t_1/\tau_{Ap}=1\times10^4$) as,

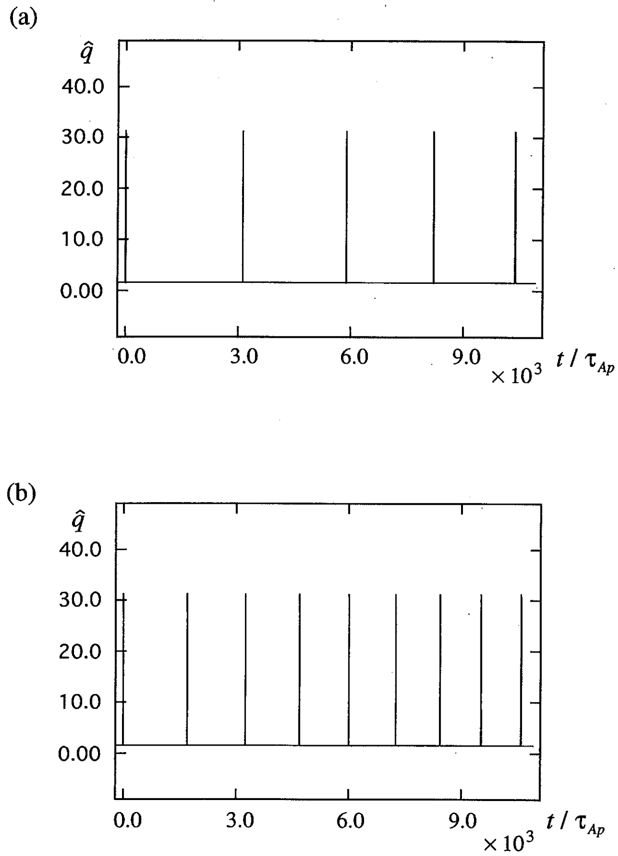

Fig. 4.7 The time evolution of the heat flux for different value of α_1; (a) $\alpha_1=2.80\times10^{-2}$ or (b) $\alpha_1=3.20\times10^{-2}$. The horizontal axis is t/τ_{Ap}. The burst of the heat flux, which is observed at $r/a=0.52$ is shown.

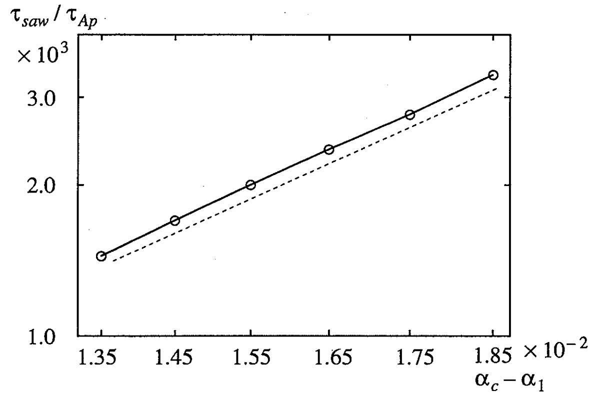

Fig. 4.6 The dependence of the period of the oscillation on the value of $\alpha_c-\alpha_1$. The axes are taken as the log-log plot. The dotted line shows the function which is proportional to $\alpha_c-\alpha_1$.

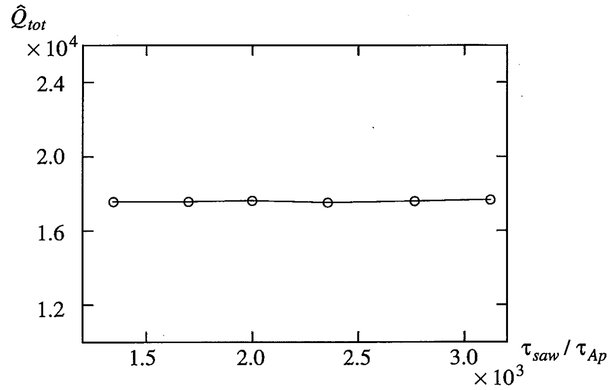

Fig. 4.8 The dependence of the time integrated exhaust energy on the oscillation period.

$$\hat{Q}_{tot} \equiv \int_{t_0/\tau_{Ap}}^{t_1/\tau_{Ap}} \hat{q} \frac{dt}{\tau_{Ap}}. \tag{4.12}$$

We examine the dependence of $\hat{Q}_{tot}$, changing the value α_1 from 2.80×10^{-2} to 3.30×10^{-2}. We find that $\hat{Q}_{tot}$ is almost independent of the period. This indicates that the heat flux per one crash is almost proportional to the period under the constant heating condition. The energy outflow exhausted by one crash is also examined. We calculate the difference of the volume-integrated plasma energy between the start and the end of the crash as,

$$\begin{aligned} \hat{q}_{tot} \equiv & \left(\int_0^{q=1} \hat{E}(\hat{r})d\hat{r}\right)_{start\ of\ the\ crash} \\ & - \left(\int_0^{q=1} \hat{E}(\hat{r})d\hat{r}\right)_{end\ of\ the\ crash}, \end{aligned} \tag{4.13}$$

where $\hat{E}(\hat{r}) \equiv T_e(\hat{r})/T_e(0) + T_i(\hat{r})/(0)$ and $\hat{r}=r/a$, respectively. From the definitions (4.12) and (4.13), $\hat{Q}_{tot}$ is expressed as $\hat{Q}_{tot}=\hat{q}_{tot}/\hat{\tau}_{saw}$, where $\hat{\tau}_{saw}=\tau_{saw}/\tau_{Ap}$. The result is shown in Fig.4.9. The exhausted energy per one crash is proportional to the period of the oscillation, $\hat{q}_{tot} \propto \tau_{saw}$. Therefore $\hat{Q}_{tot}$ is independent of τ_{saw}.

The temperature profiles of before and after the crash are shown in Fig.4.10. The global temperature profile is affected a little by the bifurcation adopted in this thesis. This is because the duration time of the M-mode is much shorter than the heat diffusive time and the region where the transition can occur is limited. In a present analysis, not the full collapse but the partial collapse is realized. The available parameter range of α has the lower limit in this model and is not sufficiently decreased for the crash front to propagate to the center of plasma. The reason is that the density is kept constant and is independent of the turbulence-turbulence transition model. The explicit expression of α is given by,

$$\begin{aligned} \alpha &= -q^2R\frac{\partial \beta}{\partial r} \\ &= -q^2R\left[\frac{\partial n}{\partial r}\left(\frac{T_e+T_i}{B}\right)+n\frac{\partial}{\partial r}\left(\frac{T_e+T_i}{B}\right)\right]. \end{aligned} \tag{4.14}$$

The term of the temperature gradient, the second term of Eq.(4.14), can decrease to zero, but the first term will not decrease to zero because we assume that the density is constant in time. This gives the lower limit for the parameter space of α. Therefore the value of back-transition condition α_1 should be chosen as,

$$\alpha_1 \geq -q^2R\frac{\partial n}{\partial r}\left(\frac{T_e+T_i}{B}\right), \tag{4.15}$$

This constrains the spatial region, where the transitions are possible.

The change of the current profile, $J(r)$, is little affected by this crash activity as is shown in Fig.4.11. This fact differs from the conventional model of the sawtooth crash based on the reconnection model [9] and is consistent with the experimental finding.

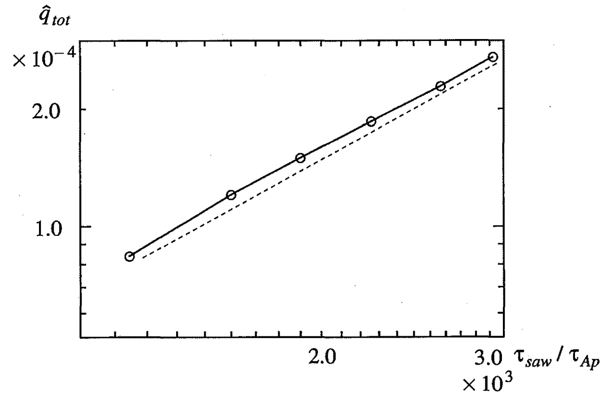

Fig. 4.9 The dependence of the energy outflow exhausted by one crash is shown. The axes are taken as the log-log plot. The dotted line shows the function which is proportional to τ_{saw}/τ_{Ap}.

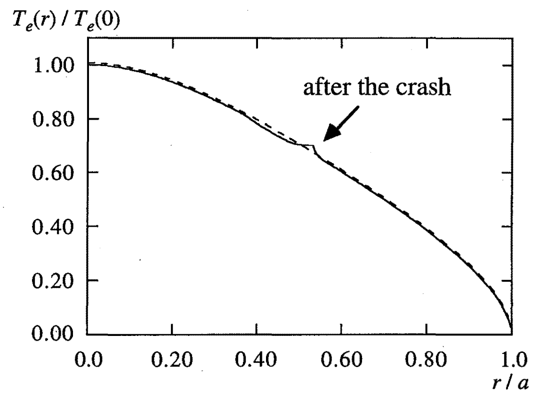

Fig. 4.10 The variation of the temperature profile before (dashed curve) and after the crash (solid curve) is illustrated.

4.4 Summary and discussion

In this chapter, we performed the transport simulation with inclusion of the turbulence-turbulence transition model. This model is described as follows. When the pressure gradient exceeds the threshold value α_c, the transition from the L-mode to the M-mode occurs and the heat conductivities are much increased. The enhanced heat flux reduces the pressure gradient. When α decreases to the threshold value for the back-transition α_1, the M-mode comes back to the L-mode. The bifurcation contains the hysteresis, i.e., $\alpha_1 < \alpha_c$. We applied this to the transport simulation and illustrated the possible dynamics of the temperature profile.

Using the model, we revealed the avalanche as the propagation of the crash front. The crash occurred at the first transition point. The heat outflow from theM-mode region made the pressure profile steeper in the neighborhood regions, and the successive M-mode transition took place when the pressure gradient exceeded the threshold value.

We studied the avalanche, which was characterized by the parameters α_c, α_1, χ_j^M and χ_j^L. We measured the propagation speed of the crash front and the crash time of the temperature profile. The velocity of the crash front was found to be order of as $v_{crash} \sim v_{Ap} \times 10^{-2}$ and was proportional to $C_M (=\chi_e^M/\chi_e^L)$, but is nearly independent of $\alpha_c - \alpha_1$.

The oscillation of the pressure gradient was observed. We attributed this toa kind of sawtooth without precursor oscillation. The hysteresis characteristic of the heat conductivity caused the periodic energy bursts. The period of the oscillation was found to be order of $\tau_{saw} \sim \tau_{Ap} \times 103$, and the pulse length was order of $\tau_{pulse} \sim \tau_{Ap} \times 101$. The duration time of the heat pulse, τ_{pulse}, increased in proportion to the period of the oscillation, τ_{saw}. The time integrated energy exhausted by the repetitive crashes was independent of the period of the oscillation (Fig.4.8). The exhausted energy per one crash was proportional to the period of the oscillation (Fig.4.9).

In this analysis, we found that 1) the L/M transition could cause the very rapid temperature disruption which was the poloidal Alfven time scale and that 2) the current profile was little changed before and after the crash. Namely, the magnetic field structure in the center was little affected and the central safety factor could remain below unity. These were consistent with the experimental results, i.e., the observed crash time was the order of 10μs and the location of the magnetic axis was little changed and the central safety factor remains below unity.

In the present analysis, the temperature full collapse could not be obtained. Becouse of the fixed density profile condition, the low limit for the parameter α was imposed. The crash front did not propagate to the center of plasma. The braided magnetic field lines possibly cause the changes not only in the heat conductivity but also in the particle diffusivity. Analysis of the time evolution of density profile to realize the fell collapse is left for future study.

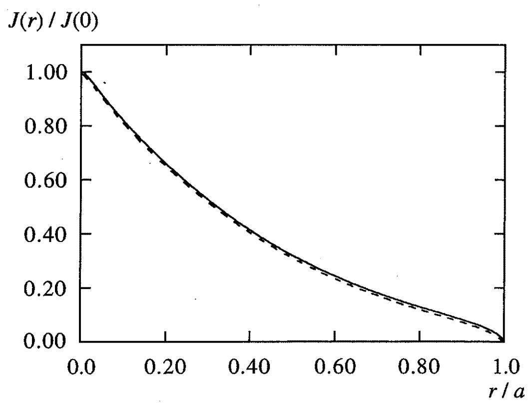

Fig. 4.11 The variation of the total current profile before (dashed curve) and after the crash (solid curve) is illustrated. The current after the crash has almost the same profile as one before the crash.

5. 1-D simulation of collapse in a giant ELM based on turbulence-turbulence transition model

In this chapter, we apply the turbulence-turbulence transition model to study a collapse at the plasma edge, which is called a giant ELM. A turbulence -turbulence transition model between the H-mode and the M-mode with the hysteresis characteristics is applied to the simulation study of edge plasma dynamics. The pressure profile development, the propagation of the bifurcation (transition) fronts and the resultant bursting fluxes are simulated. The appearance of a pivot point in the pressure profile, an avalanche followed to the transition front propagation, and the evolution of the burst are shown.

5.1 Introduction

The burst of ELM has been often observed when the edge pressure gradient approaches to the critical β value. Termination of transport barrier has usually been discussed based on the linear MHD stability [5, 6]. However, the argument of the linear MHD stability could not explain the sudden increase in the magnetic fluctuation whose time scale is order of 10 μs. The details are discussed in section 2.1.

Recently a turbulence-turbulence transition model between the H-mode and the M-mode has been proposed to explain a giant ELM [21]. The transport bifurcation takes place between the self-sustained turbulence of the electrostatic mode in the presence of the electric field shear [34] (H-mode) and the magnetic braiding mode [19] (M-mode). The M-mode transport is caused by the microscopic pressure-gradient-driven turbulence, and it reduces to the one analyzed by Rechester and Rosenbluth [13, 14] in a static magnetic field case.

In Chapter 4, the turbulence-turbulence transition model between the L-mode and the M-mode is applied to explain the sawtooth crash in the core plasma [20]. The 1-dimensional transport simulation has been performed to study the crash dynamics inside the $q=1$ surface of the plasma [25]. The crash of the temperature and the propagation of the crash front are realized.

We, here, apply the turbulence-turbulence transition model to the edge plasma and perform the simulation study of the giant ELM dynamics. The enhanced transport gives rise to a collapse of temperature profile accompanied with an avalanche process. Due to the enhanced heat flux in the M-mode region, a successive transition from the H-mode to the M-mode occurs, if the normalized pressure gradient α exceeds the threshold value, α_c. This crash propagates and the M-mode region spreads rapidly, i.e., an avalanche. In the region where the M-mode governs the transport, α is decreased due to the rapid outflow of heat flux. This process may reveal the plasma dynamics into the state with a global stochasticity. After the depletion of α to α_1 ($\alpha_c > \alpha_1$), the back-transition takes place and α starts to increase again. The process repeats itself.

The organization of this chapter is as follows. In section 5.2, the model of the transport simulation is described. The simulation results are given in section 5.3. The temporal evolution of the pressure profile shows the existence of pivot point in the very early stage of the collapse. The movements of the crash fronts and the pivot point are analyzed in detail. The dependence of the period of the oscillation is examined. Summary and discussion are given in section 5.4

5.2 Model of 1-dimensional energy transport

We include the modeled heat conductivities with hysteresis into the 1-dimensional energy transport equation. We solve the temporal development of the temperature profiles. The density profile and the mean magnetic field are fixed in time. The radial energy transport equation is

$$\frac{3}{2}\frac{\partial}{\partial t}\{n(r)T_j(r,t)\}=\frac{\partial}{\partial r}\left[\chi_j\frac{\partial}{\partial r}\{n(r)T_j(r,t)\}\right], \tag{5.1}$$

where n_j, T_j and χ_j are the density, the temperature and the heat conductivity, respectively, and j denotes the particle species ($j=i$, e). The turbulence-turbulence transition model of χ_j is introduced. We assume, for the simplicity, that the heat conductivity in the H-mode, χ^H, or in the L-mode, χ^L, is constant and independent of other parameters. The electron and ion heat conductivities in the M-mode are obtained in [21] as, $\chi_i^M=\sqrt{m_i/m_e}M\chi^H$ and $\chi_e^M=\sqrt{m_i/m_e}M\chi_i^M$, where M is parameter which indicates the effective stochastization. The threshold values of the bifurcation are defined that when the pressure gradient α exceeds α_c, the transition from the H-mode to the M-mode occurs, and when the value of α reduces to α_1, the back-transition from the M-mode to the H-mode occurs,where α is defined as $\alpha\equiv -q^2Rd\beta/dr$ and q, R and β are the safety factor, the major radius and the beta value, respectively. The threshold values, α_c and α_1, are the functions of magnetic well, the aspect ratio R/a and the shear parameter s. Here, however, we assume that the threshold values, α_c and α_1 ($\alpha_c > \alpha_1$), are given to be numerical constants. The hysteresis characteristics of the heat conductivity are shown in Fig.5.1 schematically. The slab region near the plasma edge is the region of interest, $-\mathrm{L}<r<0$.

Figure 5.2 shows the schematic configuration of the edge plasma. The conditions for the simulation are as follows. We choose the medium size standard tokamak parameters as follows: the major and the minor radii are $R=1.3m$, $a=0.35m$, the toroidal magnetic field is $B_T=1.3T$. We take $L=0.1m$. The density is assumed to be quasi-neutral, $n(r)\equiv n_e(r)=n_i(r)$, and is considered as the linear function of r,

$$n(r)\equiv\frac{n(0)-n(-L)}{L}r+n(0)\ , \tag{5.2}$$

where $n(-L)=2.0\times10^{19}m^{-3}$ and $n(0)=5.0\times10^{18}m^{-3}$ are used for this study. The safety factor is also assumed to be the linear function of r, with $q(-L)=1.2$ and $q(0)=2$ for convenience. The choice of these q values dose not change the essential results of this study. The temperatures at the plasma surface ($r=0$) are chosen to be constant as $T_e(0)=T_i(0)=50eV$. The heat flux from the core plasma ($r=-L$) is kept constant as $Q=Q_{in}$. The background heat conductivity is assumed as $\chi^L=1.0m/s^2$. The input heat flux Q_{in} is chosen to keep the temperatures as $T_e(-L)=0.34$ keV, $Ti(-\mathrm{L})=0.30keV$ at $r=-L$ under the background heat conductivity, that is, $Q_{in}=1.97\times10^4$ $Jm^{-2}s^{-1}$. The value of $T_e(-L)$ and T_i $(-L)$ are chosen to be reasonable for this size of tokamak. The model H-mode heat conductivity, χ^H, is imposed at the region from $r_1=-0.03m$ to $r_0=0m$. And χ^H is assumed as the parabolic function of r, which simulates the radial electric field profile (see Eq.(2.13)) as,

$$\chi^H(r)=-\frac{\chi^L-\chi^H_{\min}}{(r_0-r_0)^2}(r-r_c)^2+\chi^H_{\min}\ , \tag{5.3}$$

whose minimum is taken as $\chi^H_{min}=0.1m2/s$ at $rc=r1/2$ (Fig.5.3). The threshold values are assumed as $\alpha_c=1.2$ and $\alpha_1=0.15$ and the numerical factor in the M-mode heat conductivities, M, is assumed as $M=0.5$ unless specified. The heat conductivity in the region $-L<r<r_1$ is assumed not be affected by the M-mode transition, Namely, we use the constant χ^L in this region. The variables are normalized as $\hat{r}=r/a$, $\hat{t}=t/\tau_{Ap}$, $\hat{\chi}=\chi\times\tau_{Ap}/a^2$, $\hat{T}=T/T_e(-L,\ t=0)$, $\hat{Q}=Q\times\tau_{Ap}/\{aT_e$

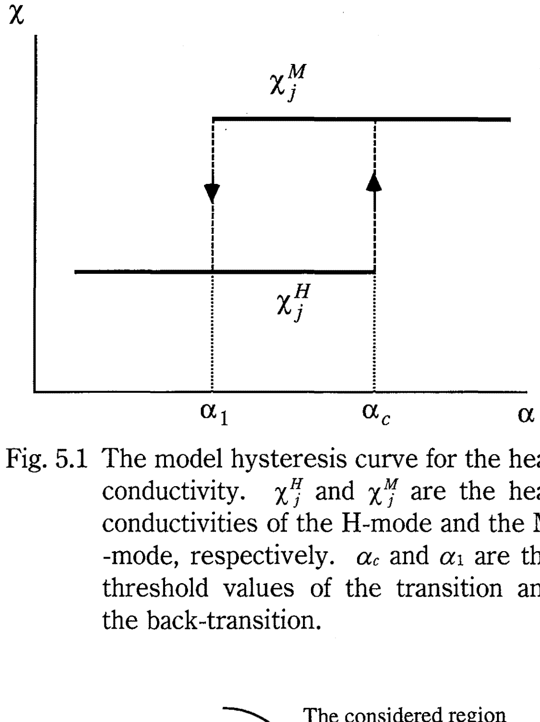

Fig. 5.1 The model hysteresis curve for the heat conductivity. χ_j^H and χ_j^M are the heat conductivities of the H-mode and the M-mode, respectively. α_c and α_1 are the threshold values of the transition and the back-transition.

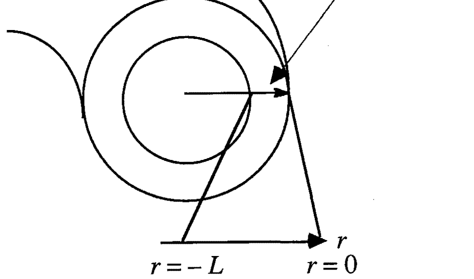

Fig. 5.2 The region of the calculateion. The edge plasma in the toloidal plasma which is indicated by the concentric shell region is considered where the poloidal symmetry is assumed.

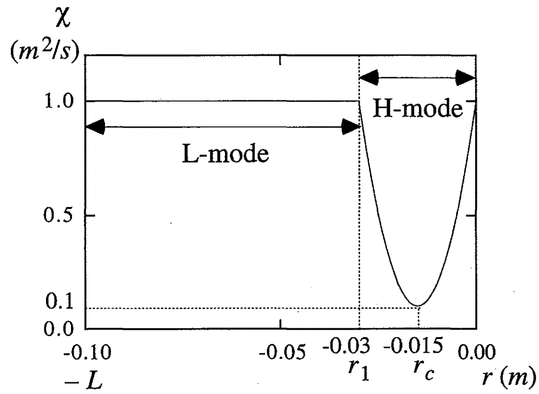

Fig. 5.3 The assumed profile of the heat conductivity. The back-ground heat conductivity (L-mode) is taken ad $\chi^L=1m^2/s$. The H-mode heat conductivity is inserted in the region from $r=0m$ to $r=r_1$ ($r_1=-0.03m$) and is assumed to be parabolic function of r.

$(-L,\ t=0)\ n(0)\}$, where τ_{Ap} is the poloidal Alfvén time ($\tau_{Ap}=a\sqrt{\mu_0 n_i m_i}/Bp$).

5.3 Temporal evolution of temperature and avalanche dynamics

In this section, the results of transport simulation are shown. We study the dynamics during the temperature crash.

The time slices of the radial profiles of pressure gradient a and $\hat{T}_e$ are shown in Figs.5.4 and 5.5. Figure 5.4 (a.1~a.4 and b.1~b.4) shows the profiles of α and $\hat{T}_e$, respectively. In Fig. 5.4 (a.1 and b.1), the dashed curves show the initial profiles of a and $\hat{T}_e$ under the background heat conductivity ($\chi_j=\chi^L$ in the whole region $-\hat{L}<\hat{r}<0$). Once the H-mode heat conductivity is put into the region $\hat{r}_1<\hat{r}<0$ to simulate the L- to H-mode transition, the slope of the temperature profile starts to be steep and the value of α increases in this region. When α reaches the threshold value, α_c, the first transition from the H-mode to the M-mode occurs at the point labeled $\hat{r}_s$ $(=\hat{r}_c)$. The solid curves in Fig.5.4 (a.1 and b.1) show the profiles

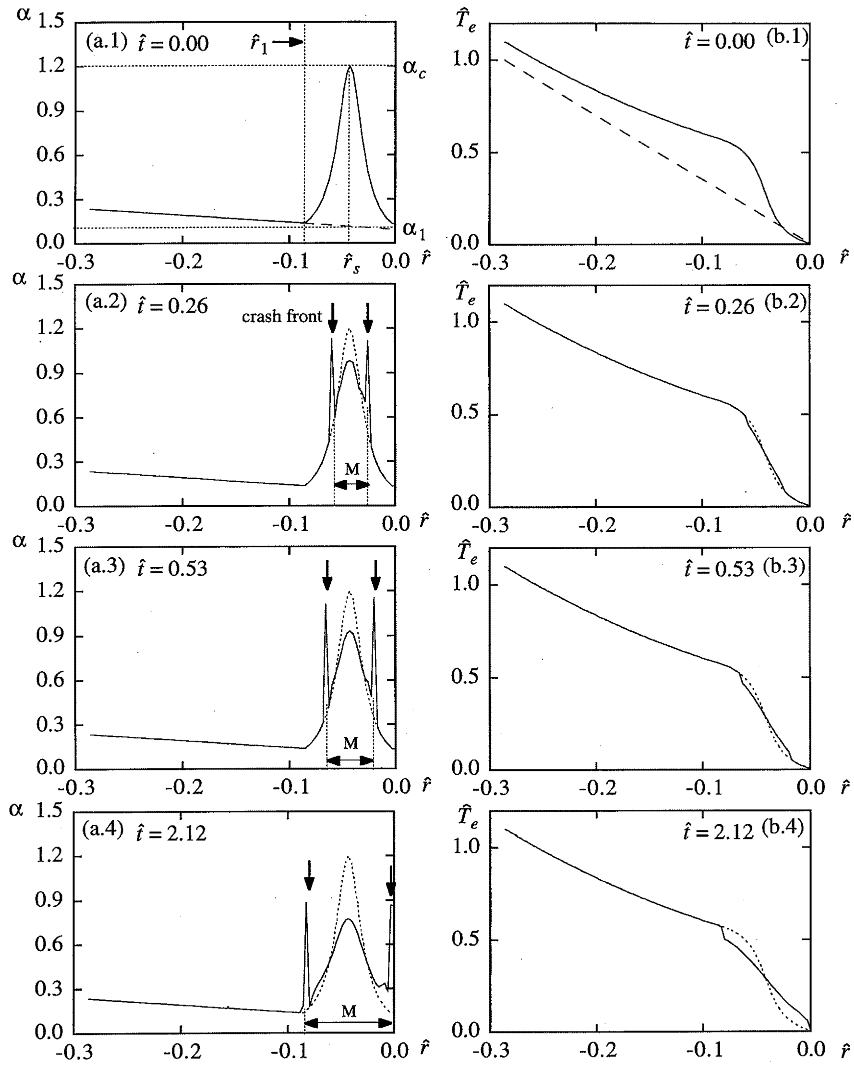

Fig. 5.4 The time slices of the profile of a and $\hat{T}_e$. The numbers 1~4 correspond to the times, $\hat{t}$=0.00, 0.26, 0.53 and 2.12, respectively. $\hat{r}_1$ is the boundary of the H-mode region. In (a.1) and (b.1) the dashed curves show the initial L-mode profile of a and $\hat{T}_e$ and in (a.2) ~ (a.4) and (b.2) ~ (b.4) the dotted curves show the α and temperature profiles of the H-mode at $\hat{t}$=0.00. The arrow ↓ indicates the crash front. The transition process starts at $\hat{r}_s$.

of α and $\hat{T}_e$ at the time when α reaches α_c, respectively. We take $\hat{t}=0$ as the start of the H- to M-mode transition process. Figure 5.4 (a.2~a.4) shows the profile of α at the time of $\hat{t}=0.26$, $\hat{t}=0.53$ and $\hat{t}=2.12$, respectively. In the region surrounded by the two peaking points of α (these points are indicated by arrows in figures), the transport mode becomes the M-mode, and the pressure gradient α decreases. At the transition boundary between the M-mode and the H-mode, α is peaked by the enhanced energy flux from/to the M-mode region. These peaked points are the crash fronts. We can see that the locations of the crash fronts move and the M-mode region expands. The crash propagates to outer and inner regions. At the time $\hat{t}=2.12$, the crash fronts reach the plasma surface and the inner boundary of the transition region. The temperature profile becomes broadened followed with the propagation of the crash fronts as is shown in Fig.5.4 (b.1~b.4) (The dotted curves in (b.2 ~b.4) show the temperature profile at $\hat{t}=0$).

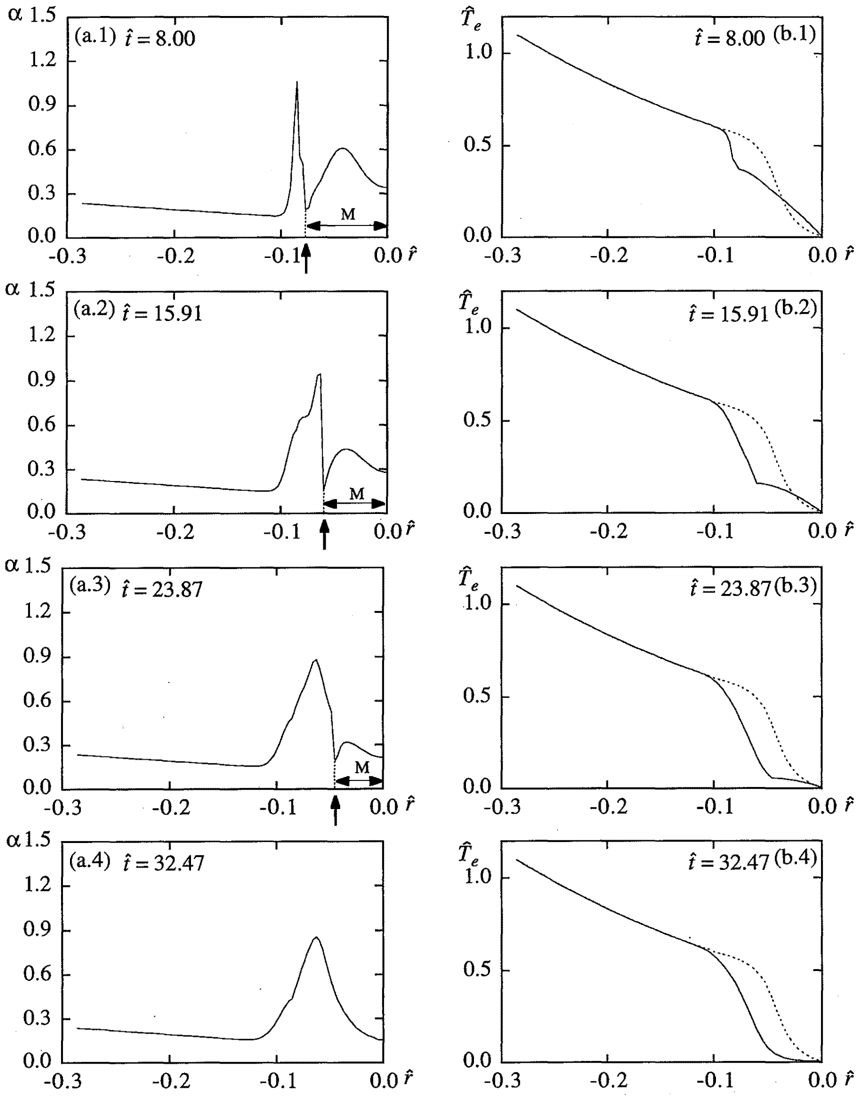

Fig. 5.5 The time slices of the profile of a and $\hat{T}_e$. The numbers 1~4 correspond to the times, $\hat{t}=8.00$, 15.91, 23.87 and 32.47, respectively. In (b.1) ~ (b.4) the dashed curves show the temperature profile at $\hat{t}=0.00$. The arrow ↓ indicates the boundary betwiin the H-mode and the M-mode (back-transition front).

We discuss the pivot point of the temperature profile. We see from Figs.5.4 (b.2~b.4) and 5.5 (b.1 ~b.4) that the pivot point in the profile of $\hat{T}_e$, which is the point where the solid curve and the dotted curve cross over with each other,appears and $\hat{T}_e$ is decreased inside of this point and $\hat{T}_e$ is increased outside due to the enhanced heat flux. The pivot point disappears during the avalanche process ($t \simeq 18$). At this point the perturbation of the temperature becomes to be zero. To show the behavior of the pivot point more clearly, we take the temperature difference between the onset time $\hat{t}=0$ and the times at $\hat{t}=0.53$, $\hat{t}=2.33$, $\hat{t}=10.61$ and $\hat{t}=18.57$ as,

$$\Delta\hat{T}_e(\hat{r},\hat{t})=\hat{T}(\hat{r},\hat{t})-\hat{T}_e(\hat{r},\hat{t}=0). \tag{5.4}$$

Figure 5.6 (a) shows the time slice of the radial profile of $\Delta\hat{T}_e$ in the region of $-0.15<\hat{r}<0$. Each curve shows the profile of $\Delta\hat{T}_e$ at the time of $\hat{t}=0.53$ (solid), $\hat{t}=2.33$ (dashed), $\hat{t}=10.61$ (dotted) and $\hat{t}=18.57$ (dotted dashed). We see that the pivot point first appears at $\hat{r}\simeq\hat{r}_s$ and propagates to outer region. Figure 5.6 (b) shows the orbit of the pivot point. This point is not clearly observed after the time about $\hat{t}=18.57$ because $\Delta\hat{T}_e$ becomes nearly zero in the outer side of the pivot point. However, the erosion of the temperature profile still continues.

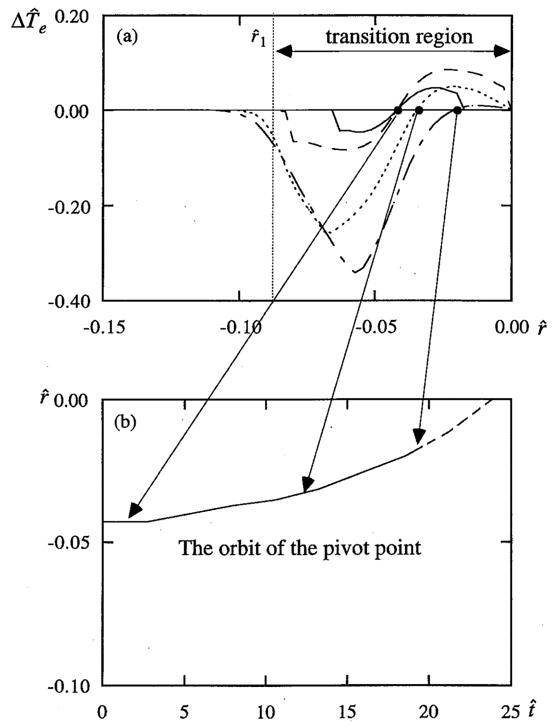

Fig. 5.6 The time evolution of the pivot point. (a) The time slice of $\Delta\hat{T}_e$ is shown. The solid curve, dashed curve, dotted curve and dotted-dashed curve are the profile of $\Delta\hat{T}_e$ at the times $\hat{t}=0.53, 2.33, 10.61$ an 18.53, respectively. The point, ●, indicates the pivot point. (b) The orbit of pivot is shown.

Next we show the time evolution of the transition boundary between the M-mode and the H-mode in Fig.5.7. The ion and the electron heat fluxes out of the plasma surface, $\hat{Q}_e$ and $\hat{Q}_i$, and the stored energy are also shown in Fig.5.7. The stored energy is defined as

$$\hat{W}_s(\hat{t})\equiv\int_{\hat{r}=-\hat{L}}^{\hat{r}=0}\hat{n}(\hat{r})\{\hat{T}_e(\hat{r},\hat{t})+\hat{T}_i(\hat{r},\hat{t})\}d\hat{r}, \tag{5.5}$$

where the energy in the edge plasma region is considered (from $\hat{r}=0$ to $\hat{r}=-\hat{L}$).

The avalanche starts at $\hat{t}=0$, that is indicated by the point marked by ●, and the crash fronts propagate outer and inner regions, which is shown in Fig.5.7 (a). The propagation of the crash fronts is terminated at the plasma surface ($\hat{r}=0$) and the boundary of the transition region at $\hat{t}=2.33$. The enhanced electron heat flux out of the plasma surface is increased rapidly which is followed by the ion's. This is shown in Fig. 5.7 (b).

When the crash front reaches the plasma surface ($\hat{t}=2.33$), the burst of the heat fluxes becomes very large. The electron heat flux $\hat{Q}_e$ is larger than the ion's $\hat{Q}$i until $\hat{t}\simeq 31$. The 1-dimensional simulation explores the detailed structures of the sawtooth crash. After the termination of the propagation of the crash front, the back-transition process starts. The M-mode region becomes narrower and disappears at the time of $\hat{t}=32.47$ and the burst terminates. Then the pressure profile gradually recovers to the original one with the time scale of $10^3\tau_{Ap}$. Under the constant heat flux from the upstream, the process repeats itself. The repetitive bursts are also obtained by this analysis as was reported in [25]

Followed with the burst of the heat fluxes, the stored energy, $\hat{W}_s$, starts to decease, which is shown in Fig.5.7 (c). The reduction of the stored energy terminates when the burst is finished. The ratio of the exhaust energy to the stored energy just before the start of the avalanche is $\Delta\hat{W}_s/\hat{W}_s=4.8\%$ in this case.

Figure 5.8 shows the dependence of $\Delta\hat{W}_s/\hat{W}_s$ to M, where M^2 indicates the ratio of the M-mode electron heat conductivity to the H-mode one, i.e., $M^2 m_i/m^2 = \chi_e^M/\chi^H$. We can see from Fig.5.8 that $\Delta\hat{W}_s/\hat{W}_s$ is almost independent of the ratio χ_e^M/χ^H. The ratio of the ion heat conductivity is proportional to M, but the contribution of the ion transport is little enough. Figure 5.9 shows the dependence of the velocity of the crash front, v_{crash}, on M. The velocity of the crash front is nearly proportional to M^2. Related with the velocity of the crash front, we define the duration time by $t_e - t_s$, where t_s and t_e denote the times of the start and the end of the energy burst, respectively. The duration time of the energy burst is the order of $10\times\tau_{Ap}$ as is seen in Fig.5.7. It is inversely proportional to the ratio M^2. The averaged exhausted power flux during the burst is roughly estimated by $(\Delta\hat{W}_s/\hat{W}_s)/(t_e - t_s)$ and is proportional to the ratio M^2.

On the other hand, Fig. 5.10 shows the relation of the total heat flux out ofthe plasma surface, $\hat{Q}_{tot}$, to M, where $\hat{Q}_{tot}$ is defined that the time integral of the heat flux during the burst as,

$$\hat{Q}_{tot} \equiv \int_{t_s}^{t_e} \{\hat{Q}_e(\hat{r}=0,\hat{t}) + (\hat{r}=0,\hat{t})\} d\hat{t}. \tag{5.6}$$

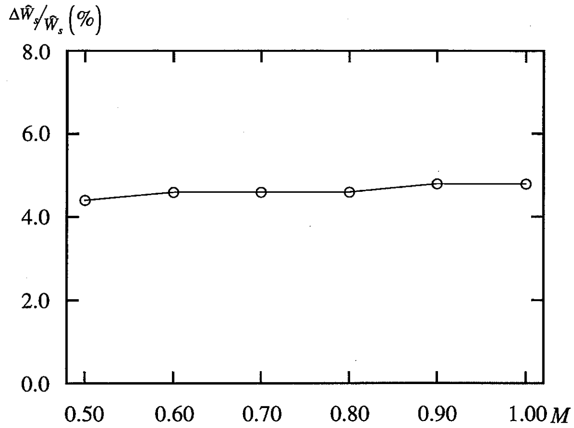

Fig. 5.8 The dependence of $\Delta\hat{W}_s/\hat{W}_s$ on M. The exhaust energy is almost independent of M.

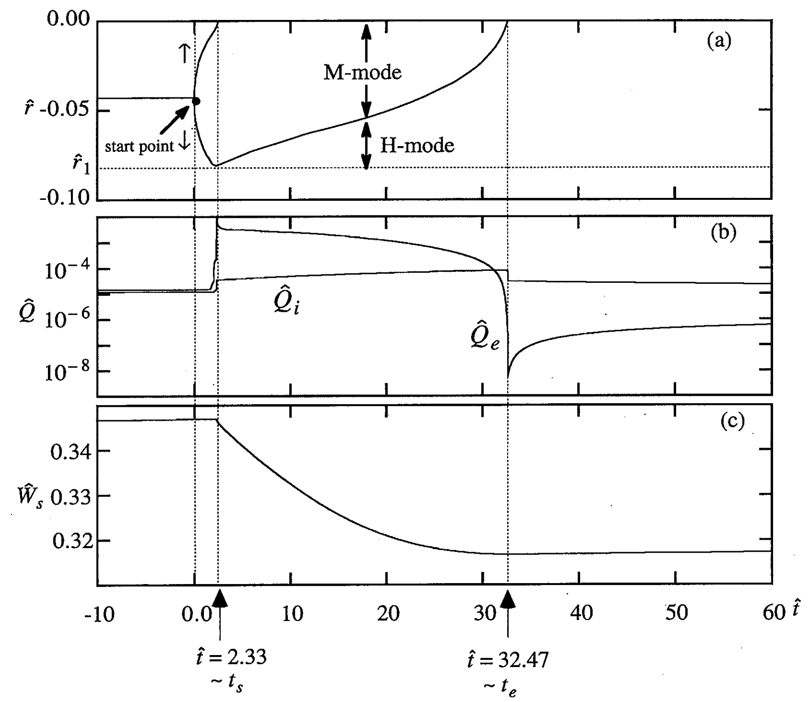

Fig. 5.7 The time evolution of (a) the radial boundary of the M-mode region, (b) the ion and the electron heat fluxes at the plasma surface ($\hat{Q}_i$ and $\hat{Q}_e$) and (c) the stored energy ($\hat{W}_s$). (a) The transition starts at $\hat{t}=0$ and the M-mode region expands rapidly. The expansion terminates at $\hat{t}=2.33$ and the M-mode region becomes narrower and disappears at $\hat{t}=32.47$. (b) The burst becomes large at around $\hat{t}=2.33$ and terminates when the M-mode region disappears, $\hat{t}=32.47$. (c) The stored energy is exhausted by the enhanced heat flux.

We can see that $\hat{Q}_{tot}$ is almost independent of M. This result is consistent with that the exhaust energy per unit time during the burst is proportional to the ratio of the heat conductivity.

5.4 Summary and discussion

In this chapter the dynamics of the edge plasma and the burst of a giant ELM were simulated. The turbulence-turbulence transition model with the hysteresis characteristics is incorporated into the heat transport equation. We analyzed the temporal evolution of the edge temperature profile by using 1-dimensional transport code.

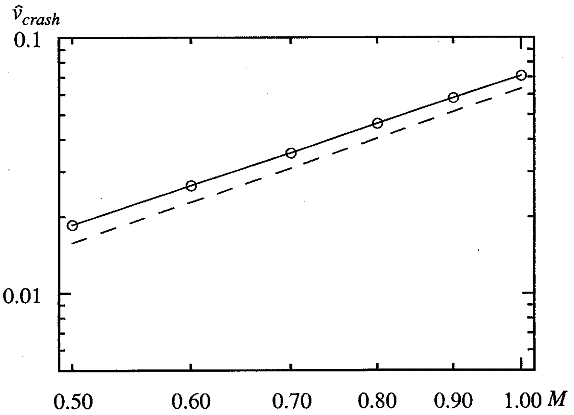

Fig. 5.9 The dependence of vcrash on M. The axes are taken as the log-log plot. The deshed line shows the function which is proportional to M^2. The velocity of the crash front is nearly proportional to M^2.

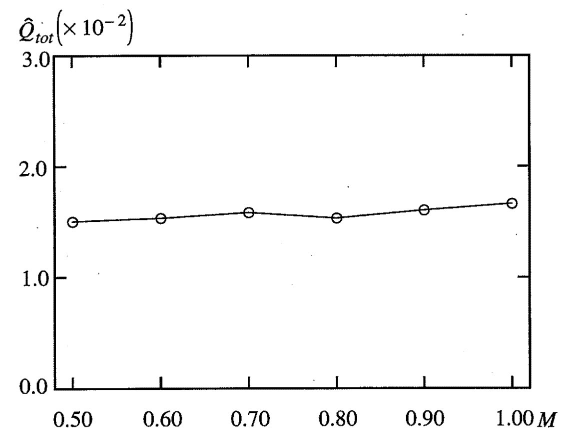

Fig. 5.10 The dependence of $\hat{Q}_{tot}$ on M. $\hat{Q}_{tot}$ is almost independent of M.

The transition from the H-mode to the M-mode occurred at a certain point in the edge layer, and the transition fronts propagated to inside and outside from this point. Followed with the propagation, the region where the crashes of the temperature profile expanded. We regard the propagation of crash front as an avalanche. The velocity of the propagation was proportional to the ratio of the electron heat conductivity for the M-mode to the one for the H-mode, $M^2 m_i/m_e$. The velocity was the order of $v_{crash} \sim 10^{-2} \times v_{Ap}$. Simulation results revealed the dynamic change of the pressure in the state with the global stochasticity.

The pivot point in the pressure profile was observed during the crash, it propagated to the outer region, and disappeared in the time about 10μs. The energy at the edge plasma was exhausted by the enhanced heat transport, which was almost independent of the ratio M. The ratio of the exhausted energy to the total stored energy in the system was about 4.8 %. The duration of the energy burst was of the order of $10 \times \tau_{Ap}$ ($\sim 10\mu$s) and was inversely proportional to M^2. The averaged exhausted power flux in a burst was proportional to the ratio M^2.

We previously applied the enhanced transport model to simulate the sawtooth crash. Similar properties were seen in the propagation of the transition front. The velocities of the transition fronts and the duration of the energy bursts had the same order of magnitude and show the similar parameter dependence on χ^M/χ^L or χ^M/χ^H. The difference was seen in the temperature profile dynamics and the amount of exhausted energy. In this analysis we assumed that the H/M transition started in the center of edge thin layer, where the H-mode was supposed to be established. After the H/M transition, the front was evacuated from the plasma surface, the back transition took place only from the inner location ($r=r_1$) as seen from Fig. 5.7(a). An extra time was necessary to re-established the H-mode transport in the whole edge region. During that time, the extra energy was exhausted due to the effect of the M-mode transport.

During a burst, the electron heat flux $\hat{Q}_e$ dominated over the ion's $\hat{Q}_i$ for most of the duration time (Fig.5.7(b)). There had been analyzed that the radial electric field was induced in the presence of the difference in the heat fluxes, $\hat{Q}_e - \hat{Q}_i$[23]. The positive electric field would be induced in our case. In this chapter, however, the consistent analysis with inclusion of the induced radial electric field was not made. Further analysis is necessary.

We analyzed the 1-dimensional system which contained the region with the localized hysteresis characteristics of the heat conductivity. The region was connected to the L-mode region. We examined the avalanche and burst phenomena. In [21], the hysteresis characteristics and the heat conductivity had the dependences on α. In this study, we considered that they were independent of α.

If this system is extended to 2-dimension, which is like a self-organized critically (SOC) system [38], a new property of the avalanche and the burst may appear. These are left for our future work.

6. Summary

In this thesis we analyzed the transport properties in a stochastic magnetic field, the temporal evolution of the magnetic stochasticity and the dynamical behavior of the temperature collapse. The system which had the hysteresis characteristics of the heat conductivity was considered.

In Chapter 3, we derived the 4×4 transport matrix. The matrix was for the fluxes of the particle, the parallel and perpendicular momenta and the energy across the mean magnetic field. It was assumed the distribution function to be a shifted Maxwellian. The 0th, the first and the second moments of the kinetic equation were taken, in which the quasi-linear effect of the magnetic fluctuation was incorporated, to derive the matrix elements.

In the stochastic region the electron flux is $\sqrt{m_i/m_e}$ times greater than that of ion, therefore the particle transport is bipolar and the ambipolar electric field is generated. The self-consistent ambipolar electric field was included in the distribution function.

We analyzed the steady state profiles of the induced electric field and the temperature, assuming a layered structure of the configuration. Namely the region, where the magnetic field became stochastic, was inserted between the non-stochastic regions. It was assumed that the particle and heat fluxes were continuous at the boundaries. In each region, the ambipolar condition was imposed on the particle fluxes. The equations for determining profiles of the ambipolar electric field and the temperature were derived. The equation was solved with the constant flux condition. The temperature profile which was flattened by the enhanced heat transport was obtained. The build up of positive radial electric field was also seen.

We also considered the effect of the $E \times B$ drift which was generated by the ambipolar electric field. As the thermodynamical force to cause the momentum flux,the velocity gradient was introduced in the presence of $E \times B$ drift. The equations of the particle flux, the momentum flux and the energy flux were combined to analyze the profiles of the density, temperature and the electric field. The $E \times B$ drift is included in the equation for the perpendicular momentum flux. It was approximated that the ion particle flux was small, since the electron flux was greater than that of ion by the factor of the ion and electron root mass ratio. The static profiles of the electron density, the temperature and the radial electric field were obtained under the constant flux condition. It was found that the radial electric field produces a viscous ion sheath. We obtained the characteristic width of the electric field generated by the ambipolar condition as $d = \sqrt{\frac{D_M m_i n(x) \langle T \rangle}{\sqrt{\pi} P^M_{1xi} eB}}$ which indicated the typical width of the ion sheath. When the momentum supply was large enough to make the characteristic width d be $d < r_s$, then the density tended to be infinity and temperature approached to zero for $d < r < r_s$, where rs was the width of the stochastic region.

In this study, the ambipolar condition $\Gamma_e \simeq 0$ was used neglecting the contribution of the ion particle flux. This constraint may be stringent since the stochastic magnetic field could influence on the ion particle flux. The divergence of the steady state solution of density was attributed to the boundary condition, i.e., the constant heat and momentum fluxes. Therefore the time evolution of transport equations with inclusion of the transport matrix under the global boundary conditions should be analyzed for future work.

In Chapter 4, we performed the transport simulation for the sawtooth crash. It was shown the dynamics of the magnetic stochastization and the temperature collapse induced by the stochastic magnetic field. When the pressure gradient exceeded the threshold value, α_c, and the amplitude of the magnetic island satisfied the Chirikov criterion, the magnetic stochasticity was generated and the heat transport was enhanced by the strong magnetic turbulence (this transport mode is called M-mode). When the pressure gradient reduced to another threshold value, α_1, the transport mode returned from the M-mode to the L-mode. The hysteresis characteristics of the heat conductivity was introduced to the 1-dimensional energy transport equation. The solution revealed an avalanche as the propagation of the crash front. The sawtooth-like oscillation of the pressure gradient was also obtained. We measured the velocity of the propagation of the crash front and the crash time of the temperature profile. The velocity of the crash front was found to be order of $v_{crash} \sim v_{Ap} \times 10^{-2}$ and was proportional to $C_M (= \chi_e^M / \chi_e^L)$, but was nearly independent of $\alpha_c - \alpha_1$. The period of the oscillation was found to be order of $\tau_{saw} \sim \tau_{Ap} \times 10^3$, and the pulse length was order of $\tau_{pulse} \sim \tau_{Ap} \times 10^1$. The duration time of the heat pulse, τ_{pulse}, increased in proportion to the period of the oscillation, τ_{saw}. The long time integrated energy exhausted by the repetitive crashes was found to be independent of the period of the oscillation.In other word, the exhausted energy per one crash was proportional to the period of the oscillation.

Little change was observed in the current profile before and after the crash,therefore the central magnetic structure was not changed by the crash.

In this study the full collapse of the temperature profile could not be obtained. The avalanche starts at $q=1$ surface, however, could not propagate to the center of plasma. This is because the density was fixed in time and the value of α had the lower limit under this condition. The braided magnetic field lines possibly caused the changes not only in the heat conductivity but also in the particle diffusivity. Analysis of the time evolution of density to realize the full collapse is left for future study.

In Chapter 5 we further applied the turbulence-turbulence transition model to the edge plasma. The dynamics of the plasma and the energy burst during a giant ELM were simulated. The 1-dimensional transport study was made for the system which had the hysteresis characteristics in the heat conductivities. The time evolution of the profiles of the pressure gradient, α, and the electron temperature were solved. The M-mode region was found to spread rapidly from the first transition point. The temperature profile crashed due to the enhanced heat transport in the M-mode region and the crash front propagated. As the result, the M-mode region extended. We obtained the propagation of the transition point as was revealed as the crash front propagation (avalanche). The velocity of the crash front propagation was found to be proportional to the ratio of the heat conductivity of the M-mode to the H-mode and to be of the order of $v_{crash} \sim 10^{-2} \times v_{Ap}$. The pivot point in the temperature profile was found to appear during the crash. It propagated to outer region and disappeared in the time about 10μs. The associated burst was examined. The exhaust energy during a burst was found to be independent of the ratio M, where the ratio of the exhausted energy to the total stored energy in the system was about 4.8%. The duration time of the temperature crash was the order of $10 \times \tau_{Ap}$ and was almost inversely proportional to M^2.

Some properties of the avalanche in a giant ELM had the similarity to ones of the sawtooth crash. That is, the velocity of the crash front was proportional to the ratio of the heat conductivities and the exhausted energy was independent of it.

In [21], the hysteresis characteristics and the heat conductivity had the dependences on α. We simplified the model and considered that they were independent of α. If this system is also extended to the 2-dimension, a new property of the avalanche and burst may appear. These are left for our future work.

In Chapters 4 and 5, it was observed that the electron heat flux was greater than that of ion during the temperature collapse. In Chapter 3, we found that the difference between the electron and ion heat flux caused the ambipolar electric field, therefore the electric field may be generated when the temperature collapse occurs. If the transport matrix obtained in Chapter 3 is connected with the1-dimensional transport code used in this study, we shall obtain the dynamic behavior of the ambipolar electric field and the associated effect on the transport. The inclusion of the off-diagonal elements in the transport matrix as well as the effect of the electric field is necessary. It is left for our future study.

Acknowledgment

One of the authors (T. K.) is indebted to Professor Y. Kawai, Professor K. Oki and Professor H. Nakasima for their useful advise and criticism in revising of the manuscript.

The authors also acknowledge fruitful suggestions and discussions from Professor K. Itoh of National Institute for Fusion Science and Dr. A. Fukuyama of Okayama University.

Finally, the author thanks to all members of his laboratory and his family for their encouragements.

References

[1] Lawson J D, 1957 *Proc. Phys.* Soc. Sec. B **70** 6.

[2] Goeler S, Stodiek W and Sasuthoff N, 1974 *Phys. Rev. Lett.* **33** 1201.

[3] Campbell D J et al, 1986 *Nucl. Fusion* **26** 1085.

[4] Edwards A W, Campbell D J, Engelhardt W W, *et al*, 1986 *Phys. Rev. Lett.* **57** 210

[5] Keilhacker M *et al*, 1984 *Plasma Phys*. Control. Fusion **26** 49.

[6] Doyle E J *et al*, 1991 *Phys. Fluids* **B3** 2300.

[7] Zohm H, 1996 *Plasma phys. Control. Fusion* **38** 105.

[8] Koide Y et al, 1994 *Plasma Phys. Control. Fusion* 36A 195 and 1994 *Phys. Rev. Lett* **72** 3662.

[9] Kadomtsev B B, 1975 *Sov. J. Plasma Phys.* **1** 389.

[10] Soltwisch H *et al*, 1986 *Plasma Physics And Controlled Nuclear Fusion Research* Vol. 1 (Vienna: IAEA) p 263.

[11] Soltwisch H, Stodiek W, Manickam J and Schluter J, 1997 *Plasma Phys. Control. Fusion* **5A** 341.

[12] Rosenbluth M N, Sagdeev R Z, Taylor J B and Zaslavskij G M, 1966 *Nucl. Fusion* **6** 297.

[13] Stix T H, 1973 *Phys. Rev. Lett* **30** 833.

[14] Rechester A B and Rosenbluth M N, 1978 *Phys. Rev. Lett.* **40** 38.

[15] Waddel B V, Carreras, Hicks H R, Holmes A J, *et al*, 1978 *Phys. Rev. Lett.* **41** 1386.

[16] Carreras B A, Hicks H R, Holmes A J, *et al*, 1980 *Phys. Fluids* **23** 1811.

[17] Lichtenberg A J, Itoh K, Itoh S -I and Fukuyama A, 1992 *Nucl. Fusion* **32** 495.

[18] Itoh S -I, Itoh K and Fukuyama A, 1993 *Nucl. Fusion* **33** 1445.

[19] Itoh K, Fukuyama A, Itoh S-I, Yagi M and Azumi M, 1995 *Plasma Phys. Control. Fusion* **37** 707.

[20] Itoh K, Itoh S -I and Fukuyama A, 1995 *Plasma phys. Control. Fusion* **37** 1287.

[21] Itoh S -I, Itoh K, Fukuyama A, *et al*, 1996 *Plasma phys. Control. Fusion* **38** 5271.

[22] Kubota T, Itoh S -I, *et al*, 1995 *Trans. Fusion Tech.* **27** 493.

[23] Kubota T and Itoh S -I, 1995 *Phys. Plasmas* **2** 3368.

[24] Kubota T, Itoh S -I, Yagi M, *et al*, 1995 *Phys. Plasmas* **2** 3368.

[25] Kubota T, Itoh S -I, Yagi M, *et al*, 1997 *Plasma Phys. Control. Fusion* to be published.

[26] Gohil P *et al*, 1988 *Phys. Rev. Lett.* **61** 1603.

[27] Zaslavsky G M and Chirikov B V, 1972 *Sov. Phys. Usp.* **14** 549.

[28] Itoh S -I and Itoh K, 1992 *Kakuyugo kenkyuu* **67** 136.

[29] Stix T H, 1978 *Nucl. Fusion* 18 353.

[30] Dubois M A, Samai A, 1980 *Nucl. Fusion* **20** 1101.

[31] Krommes J A, Oberman C and Kleva R G, 1983 *J. Plasma Phys* **30** 11.

[32] Kaw P, Valeo J and Rutherfordo P H, 1979 *Phys. Rev. Lett.* **43** 1398.

[33] Boozer A, 1986 *J. Plasma Phy* **35** 133.

[34] Itoh S -I and Itoh K, 1988 *Phys. Rev. Lett.* **60** 2276.

[35] Itoh S -I, 1990 *J. Phys. Soc. Jpn.* **59** 3431.

[36] Morishita T, Fukuyama A and Furutani Y, 1988 *J. Phys. Soc. Japan* **57** 1238.

[37] Hinton F L and Hazeltine R D, 1976 *Rev. Mod. Phys.* **48** 239.

[38] Bak P, Tang C and Wiesenfeld K, 1988 *Phys. Rev. Lett.* **59** 381.